8-9-2014

Thermal Analysis of High Pressure Micro Plasma Discharge

Mostafa Mobli
University of South Carolina

THERMAL ANALYSIS OF HIGH PRESSURE MICRO PLASMA DISCHARGE

by

Mostafa Mobli

Bachelor of Science
University of Tehran, 2012

Submitted in Partial Fulfillment of the Requirements

For the Degree of Master of Science in

Mechanical Engineering

College of Engineering and Computing

University of South Carolina

2014

Accepted by:

Tanvir Farouk, Director of Thesis

Jamil Khan, Reader

Chen Li, Reader

Lacy Ford, Vice Provost and Dean of Graduate Studies

DEDICATION

To my wife, my parents, for their endless love, support, and encouragement, and to my professor at U of SC.

ACKNOWLEDGEMENTS

I would like to express my deepest appreciation to my advisor Dr. Tanvir Farouk for his guidance, patience and support. Thank you for forcing me to look at research and my work in different ways. Thank you for believing in me and helping me stand up after every fall. Your support was essential to my success here.

I would like to thank my committee members, Dr. Jamil Khan and Dr. Chen Li for their invaluable advice and help throughout my research.

I owe my deepest gratitude to my parents, for their endless love, support, and encouragement. No words can describe my love to you both.

I would like to thank my beautiful wife Sara Nakhi for her invaluable friendship and support in difficult times and my fellow graduate students for their friendship and assistance. I will always remember the great times we had.

At last, I would like to thank the members of my department, Mechanical engineering. The faculty, staff, and students made my stay in Columbia a great experience.

ABSTRACT

High pressure micro plasma discharge has been at the center of interest in recent years, because of their vast applications, ease of access and cost efficiency. This attributes to atmospheric discharges that are generated in ambient conditions and therefore can be readily applicable to everyday use. The absence of vacuum makes these high pressure discharges to be inexpensive to operate. Despite the ease of operation, the high pressure is a source of enhanced gas heating as the gas temperature cannot be controlled by diffusion alone. Gas heating is therefore an important factor when it comes to the simulation of high pressure micro plasma discharge, unlike their low pressure counterpart where the heat generation is almost negligible. Low pressure discharge due to their low degree of collisionality generates ionic species and electrons at small concentrations, whereas high pressure discharge due to their higher gas density produces ions and electrons at higher concentrations which is a direct consequence of increase collision. The higher gas density and consequential large concentration of ionic species and electron contributes directly to higher heat generation rates. .

In this thesis the gas temperature transport of high pressure micro plasma discharge has been studied with a special focus on the heat source terms, temperature boundary conditions, temperature distribution in the solid phase electrodes and the gas phase and their overall influence on the plasma

characteristics. For this purpose a multi-physics mathematical model has been developed that comprised of a plasma module, neutral gas temperature module, external circuit module and conjugate heat transfer module. The plasma module consisted of conservation of the different ionic, electronically excited species, radicals, neutrals and electrons, conservation of the electron temperature, and electric field. The external circuit module resolved the coupled driving circuit comprised of a voltage source, ballast resistor and capacitance. A detailed gas phase chemical kinetic model was also implemented. One-dimensional simulation has been performed to study the effects of the neutral gas temperature on a micro plasma discharge operating in the *"abnormal"* glow mode. In addition, two dimensional simulation has been conducted to simulate the *"normal"* glow regime of a micro plasma discharge that has multi-dimensional spatial dependence. The effects of conjugate heat transfer on the gas temperature distribution and the overall plasma characteristics i.e. the voltage-current curve and electron number density has been investigated. The conjugate heat transfer is found to significantly affect the plasma behavior. Finally a temporally varying temperature boundary condition has been proposed that reduces the computational overhead but resolves the conjugate heat transfer effect with reasonable accuracy.

TABLE OF CONTENTS

LIST OF TABLES

LIST OF FIGURES

List of Symbols

n_e	Electron number density.
n_+	Ion number density.
N_m	Neutral number density.
n_*	Excited number density.
n_e	Electron density.
n_i	Species number density.
n_ε	Electron energy source term.
t	second.
Γ_i	Species flux.
Γ_e	Electron flux.
Γ_+	Ion flux.
Γ_*	Excited species flux.
Γ_m	Neutral species flux.
D_e	Electron diffusivity.
D_+	Ion diffusivity.
D_m	Neutral species diffusivity.
D_*	Excited species diffusivity.
μ_i	Species mobility.
μ_e	Electron mobility.
μ_+	Ion mobility.

μ_m Neutral species mobility.

μ_* Excited species mobility.

R_i Source term.

R_e Electron source term.

R_+ Ion source term.

R_* Excited species source term.

R_m Neutral species source term.

s_ε Electron energy source term.

E Electric field.

ΔH Enthalpy change.

V Discharge voltage.

z_i Charge number.

ρ Gas density.

C_p Gas thermal capacitance.

T_g Gas temperature.

T_e Electron temperature.

j_+ Ion current density.

I_b Total current.

Q_{gas} Energy loss by reactions.

T_s Solid temperature.

h Heat transfer coefficient.

K Gas conductivity.

K_s Solid Conductivity.

$v_{e,th}$ Electron thermal velocity.

$v_{i,th}$ Ion thermal velocity.

ϵ_i Mean energy.

R_b Ballast resistance.

C_{par} Parasitic capacitor.

V_P Power supply voltage.

Γ Incomplete gamma function.

$\sigma_k(\varepsilon)$ Cross section.

x_i Mole fraction.

P Pressure.

k Boltzmann constant.

k_i Reaction rate of every species.

List of Abbreviations

CHT ..... Conjugate Heat Transfer

IJH ..... Ion Joule Heating

LUT ..... Lookup Tables

SF ..... Stepping Function

VI ..... Voltage Current

CHAPTER 1

BACKGROUND

1.1. Introduction

Gas discharge, also known as plasma discharge, refers to the process of discharge of a capacitor into a circuit including a gap between two electrodes filled with gas. With sufficient power supply voltage, breakdown occurs which leads to the formation of an ionized state of the gas [1]. The break down voltage and the voltage current curve are among the main characteristics of the discharge denoting the region of operation. The plasma characteristics are strongly dependent upon geometry of the electrodes, the inter-electrode separation, electrode material, feed gas, external circuit and the operating pressure. There are many applications to gas discharges, such as biomedical (skin treatment), metallurgical and material processing (etching and film deposition), aeronautical (motion control on wings), propulsion (Hall and Ion thrusters) etc. [2-13]. Besides the various gas discharge applications, there are numerous types of discharges which can be classified by the type of power sources such as Dielectric Barrier Discharge (DBD), Radio Frequency (RF) Discharge; the thermodynamic state such as DC driven glow discharge – non-equilibrium state, DC driven arc discharge – equilibrium state; the mode of operation such pulsing streamer discharge, steady corona discharge etc. The major focus of this thesis is glow discharge operating in the "*normal*" and

"*abnormal*" mode at atmospheric and higher pressures. Typically glow discharges are generated at low pressures having macro scales. But these types of discharge limits the applications of such plasmas as they expensive operating cost due to the necessity of vacuum pumps [14]. Atmospheric pressure plasma discharges are a potential alternative.

Atmospheric glow discharge is not the only known atmospheric discharge, DBDs, Corona and Arc discharges are also generated at atmospheric pressure. The gas temperature in all atmospheric discharges is a huge concern and therefore plays an important role in the discharge characteristics. At low pressure discharges, due to large scales and lower gas heating, heat diffuses rapidly and therefore gas temperature does not change a lot. While in high pressure discharges, gas heating increases dramatically and so does the gas temperature [15, 16]. As spatial dimensions are reduced to micron size the gas heating is known to have enormous effect especially in high pressure micro plasma discharge. The effects of high gas temperatures is not only limited to the gas phase, it has the potential to affect the electrodes as well. Figure 1.1. and figure 1.2. depicts the effects of gas temperature on the electrodes material, which can include material distortion, erosion and meltdown of the electrodes [17].

Due to importance of gas heating, there has been a growing research interest in analyzing and determining the neutral gas temperature of plasma discharges. The main source of gas heating is known to be the ion joule heating and the enthalpy change due to heavy particle reactions [15 -17]. In most researches conducted on the analysis of gas temperature in plasma discharges

no attention has been given to the contribution of energy transport at the electrodes, nor its influence on the gas phase temperature distribution rather a Dirichlet boundary condition of constant temperature is assumed. To the best of our knowledge, previous works on plasma discharge modeling have excluded the effects of conjugate heat transfer. In this thesis the conjugate heat transfer effect on plasma discharge has been studied by two approaches – a direct computation approach of the conjugate heat transfer and a “revised” boundary condition approach. In the computation approach the temperature both in the gas and solid phase are resolved by employing boundary conditions and interface conditions. The “revised” boundary condition relies on an analytical approach where the boundary temperature varies temporally according to the incoming heat flux from the plasma domain. Neither of these approaches have been utilized in plasma discharge simulations, the conjugate heat transfer approach is vastly used in combustor and heat exchanger design where wall temperature is critical for optimum performance [18, 19].

1.2. Literature review

1.2.1 Low and High Pressure Glow Discharge

One of the earliest computational study on the subject of low pressure glow discharge have been done by Lymberopolous and Economou [4]. They studied argon discharge for a parallel plate configuration employing a continuum based fluid model. They had studied the effects of metastable atoms on the argon glow discharge characteristics. Due to slow response time of metastable

atoms, they employed an acceleration scheme based on the Newton-Raphson method to reduce the convergence time. Their model included the continuity equations, flux calculation based on a drift-diffusion approximation and electron energy balance. The Poisson's equation was solved to compute the self-consistent electric field. The acceleration scheme has shown to be useful for carrying out coupled glow discharge and neutral-transport-reaction simulations where detailed chemical kinetics are considered.

Guerra et al. [20] conducted kinetic modeling of low-pressure nitrogen discharges where the effects of the vibrationally excited nitrogen molecules on the gas heating, shape of electron energy distribution function, creation and destruction of electronically excited states and afterglow emissions were investigated. Their research extended the analysis on other metastable molecules and has shown to be effective on ionization and other characteristics of the discharge in nitrogen

In the early twenty first century the development of micro plasma discharge triggered a number of experimental and theoretical studies. Wang, et al. [11] proposed a one dimensional fluid model and performed numerical simulation of a DC driven micro plasma discharge operating in helium at atmospheric pressure. One of their focus was characterizing the plasma discharge. Voltage current characteristics curve, electron density profiles and temperature distribution was obtained. Ion Joule heating and energy transfer through elastic electron-neutral collisions was identified to be the major contributor to the neutral gas temperature. They found that high pressure micro

scale discharges resembles low pressure macro scale discharges under scoring the importance of pressure x electrode separation distance “pd” scaling rule.

Farouk and coworkers [6] simulated high pressure micro discharge employing a hybrid model. They studied the “normal” glow regime for a pin-plate configuration. This model was able to predict the flat voltage current characteristics of a normal glow discharge, in which the discharge voltage does not change with increase in current. The whole phenomena is diffusion limited and occurs due to the fact that the current density remains constant in the “*normal*” glow and total current increases because of changes in discharge area over the cathode.

Farouk conducted another study on the high pressure micro discharge in diatomic gas - hydrogen [7]. Their study indicated that unlike monatomic gases the neutral gas heating is dominated by vibration-translation relaxation rather than ion joule heating. They further showed that the “*normal*” current density of high pressure micro plasma discharge is a temperature scaled value of its low pressure counterpart. Secondary electron emission was found to have inverse relation with discharge voltage.

In addition to the various numerical works a large number of experimental studies on micro plasma discharge has been conducted by numerous researchers. Wang and colleagues [21] investigated a helium micro plasma discharge experimentally. Optical emission spectroscopy measurements were performed. Spatial gas temperature distributions were obtained. The measured gas temperature showed a peaking near cathode. In support to their

experimental work their numerical model determined that the observed gas temperature profile was due to the higher ion joule heating rate inside the cathode sheath. However they employed isothermal boundary with preset initial condition. Therefore their model was not able to predict the difference of gas temperature in the anode and cathode.

Staack and coworkers [22, 23] performed a comprehensive experimental study on high pressure micro plasma discharge in atomic and molecular gases. They found that the discharge voltage of "*normal*" glow discharge scales with effective density. This hypothesis was validated by their experimental data for different atomic and molecular gases. They measured the rotational, vibrational gas temperature of the discharge with optical emission spectroscopy and reported high gas temperatures for micro plasma discharge operating in diatomic feed gases e.g. nitrogen and hydrogen.

1.2.2 Conjugate Heat Transfer

Conjugate heat transfer has been widely used in combustion, heat exchanger and gas turbine design applications. In general, conjugate heat transfer (CHT) is required in in every part of engineering where there is a solid fluid interaction. Pantazis, et al. studied conjugate heat transfer effects from a low temperature nitrogen gas to a thermocouple [24]. For this purpose, they employed a three dimensional transient model to characterize the thermocouple in terms of response time. They used OpenFOAM software to analyze their model. For the conjugate heat transfer part they applied a time dependent

boundary condition at the solid fluid interface. This temperature was assigned to the entire thermocouple surface since conditions were such that the entire thermo couple could be assumed to be like a small line element where radial temperature is the same over the cross section.

ontanesi and Giacopini [25] applied the conjugate heat transfer analysis to a V6 diesel engine to estimate and optimize the combustion engine cooling jacket. For this purpose, they had developed a CFD and FEM model of the engine to couple the structural and thermo fluid analysis of the engine. They employed the heat continuity boundary condition to include the effects of conjugate heat transfer on the coolant and to determine the coolant temperature distribution and phase change.

Duchaine and his colleagues performed a comprehensive study of conjugate heat transfer on turbine blade [26]. They introduced a coupling strategy between conjugate heat transfer analysis and large eddy simulation (LES). The coupling strategy is based on the heat continuity method where heat flux and temperature at the solid fluid interaction are assumed to be equivalent on both sides. They introduced the concept of coupling relaxation parameter (CPR), which related the boundary heat flux and boundary temperature resulting in a mixed boundary condition for the entire structure.

Veeraragavan and Cadou [27] studied the flame speed prediction in planar combustor where the conjugate heat transfer at the combustor wall was resolved. They had developed an analytical model for flame stabilization by solving heat diffusion equation in solid and fluid part. They also explored the

effects of heat loss to environment as well as wall thermal conductivity and wall geometry on the burning velocity and extinction. In their earlier work [28], they had developed an analytical model for the general embedded heat source applied to parallel flow. In this model, they had not considered the heat loss to the environment and solid wall boundary was considered to have Dirichlet boundary condition, but the solid fluid interface was again a heat continuity boundary condition.

Shen, Sun and Xia has studied the effects of conjugate heat transfer in a gap-cavity-gap structure [29]. They treated the boundary condition as a heat continuity boundary condition, where the fluxes are the same. In their method, radiation heat transfer as well as conduction and convection heat transfer is considered. With a first order approximation on the flux balance, boundary temperature is computed and solved numerically. The accuracy of this method is obtained by coupling between the convergence residual of fluid and solid domains.

Despite the numerous CHT study in combustion, heat exchanger and gas turbine application our literature survey failed to provide any literature that reports CHT analysis of plasma discharge. Coupled CHT and plasma discharge study therefore remains to be a topic of extreme interest, importance and relevance.

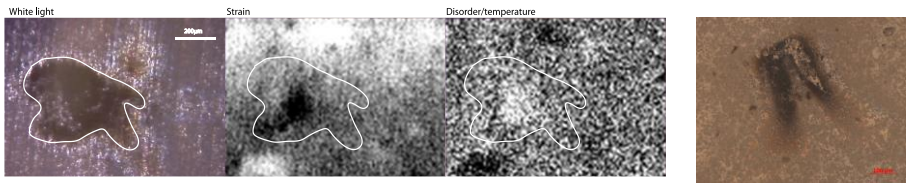

Figure1.1. Pd evaporated metal on the cathode side, hot spot of 200 um seen in temperature and strain maps, (Courtesy Dr. David Staack Texas A&M University)

Figure. 1.2. Electrode life time, Pd Electrodes (50 μm diameter) N2 Gas, 1 mA (~0.5 W) steady state for 10(+) minutes, (Courtesy Dr. David Staack Texas A&M University).

CHAPTER 2

MATHEMATICAL MODEL

In this chapter a detailed description of the micro plasma discharge model is discussed. A continuum based fluid model was employed to obtain the discharge characteristics. The model included conservation equation for all the species (electron, ions and neutrals), the energy conservation for electron, Poisson's equation for electric field and energy conservation for the neutral gas temperature. Different species source term and reaction rates calculations were obtained from a pre-assumed Maxwellian electron energy distribution function. All the discharge calculations and simulations in this thesis are conducted for a parallel plate electrode configuration filled with a mixture of helium – nitrogen. In most cases the mixture had a composition of 99.98% He and 0.02% N_2. Assumptions made in this modeling are as follows:

1. All heavy particle temperatures are considered to be equal.
2. Electron transport parameters and electron induced reaction rates are obtained from a Maxwellian electron energy distribution function.

2.1. Schematic of the computational geometry

Schematic of the computational geometry is presented in Figure 2.1. The electrical circuit consists of a power supply parallel to a capacitor and the

discharge domain. The power supply is in series with the ballast resistance which is required for limiting the discharge current. The capacitor represents the parasitic capacitance of the circuit. Figure 2.1. depicts the electrical circuit applied to discharge domain, in all cases, the parasitic capacitance is considered to be 0.01 pF, power supply is set to be either 500 V or 1000 V, the ballast resistance was varied in between 1 kΩ - 30 MΩ.

The discharge has an inter electrode spacing of 200 um in a parallel plate configuration as depicted in Figure 2.2. For the conjugate heat transfer analysis, the electrodes length is set to be 5000 um, which has a cylindrical shape, and the radius is fixed at 440 um (the cross sectional area is 0.006 cm^2). The electrode material is chosen to be molybdenum to be consistent with published experimental data [17]. Those experimental data are used for model validation. The effects of different electrodes materials on the discharge characteristics have also been investigated.

2.2. Governing Equations and Chemical Kinetics

2.2.1. Governing Equations

The governing equation consists of species conservation equations for all the different species, energy conservation for electrons

The species equation for the charged species has the following form:

$$\frac{\partial n_i}{\partial t} + \nabla . \Gamma_i = R_i \tag{2.1}$$

Where n_i is the charged particle density, Γ_i is the charged particles flux, R_i is the source term; which is essentially the sum of all reaction rates contributing

to i^{th} species, where charged species are produced and consumed due to ionization, recombination, or heavy particle reactions such as Penning ionization.

The species flux is calculated based on a drift-diffusion approximation having the following expression:

$$\Gamma_i = -(\mu_i . E) . n_i - D_i . \nabla n_i \quad (2.2)$$

Where, μ_i is the charged species mobility, E is the electric field and D_i is the charged species diffusivity. The transport properties for the different charged species are summarized in Table 2.3.

The conservation equation for the electronically excited species and neutrals have the following form:

$$\frac{\partial n^*}{\partial t} + \nabla . (D^* . \nabla n^*) = R^* \quad (2.3)$$

$$\frac{\partial n_m}{\partial t} + \nabla . (D_m . \nabla n_m) = R_m \quad (2.4)$$

Where, n^* and n_m are the excited particles number density and neutral number density respectively, D^* and D_m are heavy particle diffusivity and R^* and R_m are sources terms which are calculated from the summation of reaction rate in which heavy particles are produced or consumed.

The electron energy conservation equation is expressed as follows:

$$\frac{\partial n_\varepsilon}{\partial t} + \nabla . \Gamma_\varepsilon + E . \Gamma_e = S_\varepsilon \quad (2.5)$$

Where the n_ε is the electron energy number density, Γ_ε is electron energy flux and S_ε is the source terms for electron energy which represents the electron energy loss or gain due to inelastic or elastic collisions.

The electron energy flux and source terms is expressed as:

$$\Gamma_\varepsilon = -(\mu_\varepsilon . \mathrm{E}) . \mathrm{n}_\varepsilon - \mathrm{D}_\varepsilon . \nabla \mathrm{n}_\varepsilon, \mathrm{S}_\varepsilon = \sum_{\mathrm{i}} \mathrm{R}_\mathrm{i} . \Delta \mathrm{H} \tag{2.6}$$

Where, μ_ε is the electron energy mobility and D_ε is the electron energy diffusivity. The energy source term is calculated by summing up the elastic and inelastic collisions reaction rates multiplied by the corresponding energy loss/gain.

The Poisson's equation is used to obtain the electric field. The Poisson's equation has the following expression:

$$\nabla . \mathrm{E} = -\nabla^2 \Phi = \frac{\mathrm{e}}{\epsilon} \left(\sum_\mathrm{i} \mathrm{z}_\mathrm{i} \mathrm{n}_\mathrm{i}\right) \tag{2.7}$$

Where, E is the electric field, Φ is the electric potential, e is the elementary charge, ϵ is vacuum permittivity, z is the charge number which is +1 for ions and -1 for electrons.

Gas temperature is obtained from the solution of the energy equation having the following the expression:

$$\rho \mathrm{C}_\mathrm{p} \frac{\partial \mathrm{T}_\mathrm{g}}{\partial \mathrm{t}} = \mathrm{k} . \nabla^2 \mathrm{T}_\mathrm{g} + \mathrm{Q} \tag{2.8}$$

Where, ρ is the gas density, C_p is the specific heat, k is the gas conductivity and Q is the power density dissipated as gas heating is the energy source term. The energy source term has the following expression:

$$\mathrm{Q} = \mathrm{j}_+ . \mathrm{E} + \mathrm{Q}_\mathrm{gas} \tag{2.9}$$

The first term in this equation accounts for Ion joule heating where j_+ is the ion discharge current density. The second term is the energy transfer during the heavy particle reactions and is obtained by:

$$Q_{gas} = \sum_i R_i \Delta H_i \tag{2.10}$$

Where R_i is the reaction rate of every reaction and ΔH_i is the change of enthalpy of every reaction.

Heat transfer in the electrodes is obtained by solving an energy equation over the electrodes and is related to the discharge domain by heat continuity boundary condition between plasma domain and electrodes. The energy equation has the following form:

$$\rho_s C_{p_s} \frac{\partial T_s}{\partial t} = k_s . \nabla^2 T_s \tag{2.11}$$

Where, $\rho_s, C_{p_s}, T_s, k_s$, are electrode density, electrode heat capacity, electrode temperature and electrode conductivity respectively.

2.2.2. Boundary Conditions

Wall boundary condition is applied for the species flux terms, wall boundary for the electron has the following expression:

$$n . \Gamma_e = \frac{1}{2} v_{eth} n_e - \sum_i \gamma_i (\Gamma_i . n) \tag{2.12}$$

Where n is normal vector of the cathode or anode pointing outwards, $v_{eth}$is the electron thermal velocity provided by $v_{eth} = \sqrt{\frac{8k_bT_e}{\pi m_e}}$, γ_i is the secondary emission coefficient from the i[th] ion species, Γ_i is the i[th] ion species at the wall. The secondary electron emission coefficients were varied from 0.11 – 0.20.

The boundary condition for all species:

$$n.\Gamma_i = \frac{1}{2} v_{ith} n_i \tag{2.13}$$

Where n is the normal vector pointing outward, v_{ith} is the species thermal velocity provided by $v_{ith} = \sqrt{\frac{8k_bT_g}{\pi M}}$ and n_i is the species number density.

The electron energy wall boundary has the following expression:

$$n.\Gamma_\varepsilon = \frac{5}{6} v_{eth} n_\varepsilon - \sum_i \gamma_i \epsilon_i (\Gamma_i.n) \tag{2.14}$$

Where, ϵ_i is the mean energy of emitted electrons from the cathode for i[th] species of ions, which is set to be 5 ev in our study [16].

Cathode is grounded, thus the electric potential is set to zero and anode electric potential is obtained from the external circuit model which has the following expression:

$$V_d = V - I_d R_b - R_b C_{par} \frac{dV}{dt} \quad (2.15)$$

Where, V is the voltage provided by power supply, I_d is the discharge current, C_{par} is the parasitic capacitance.

2.2.3. Temperature Boundary Condition

All recent researches conducted on high pressure micro plasma discharge have considered the effect of heat generation inside the plasma [10, 14, 16], as mentioned in literature review section. In their work, the isothermal boundaries have been used to solve the energy equation within the plasma domain. While this assumption seems to be far away from what is really happening in the discharge, due to ion joule heating, the boundary temperature is changing over time. Moreover, the ion joule heating is larger near the cathode than anode which has the potential to make the cathode hotter than the anode. The isothermal boundary condition omits these effects and applies an artificial temperature distribution to the discharge, which can be cooler or hotter than the actual discharge temperature depending on the assigned temperature magnitude at the boundaries. In this thesis, in addition to determining the effects of pressure, a full detailed analysis has been conducted on the temperature boundary condition of the domain. The heat transfer in the electrodes has been added to the heat transfer analysis in order to let the boundary's temperature

change freely. Assigned boundary condition is heat continuity. This approach is the classical conjugate heat transfer (CHT) simulation approach and is believed to be representative of the most realistic of situations. CHT can capture the temperature difference at the two electrodes as well as the change in boundary temperature.

Since the CHT approach increases the numerical expenses a new temporally varying boundary condition is also proposed. This boundary condition is obtained from the analytical solution of conduction heat transfer in a semi-infinite solid exposed to a varying heat flux at the boundary. Detailed description of the boundary condition is provided in the following chapter.

2.2.4 Chemical Kinetics

The chemical kinetics consisted of 11 electron impact reaction, 14 heavy particle reactions and 7 surface reactions. Species included are electron, ionic species (He^+, He_2^+, and N_2^+), excited species (He (2^1S), He (2^3S), metastable (He^*, He_2^*)) and neutral species (He, N_2). The reactions considered in the simulations are summarized in in Table. 2.1.

Reaction rates for some of the electron impact reactions are obtained from the cross section data assuming the electron energy distribution function (EEDF) to be Maxwellian. For these specific cases the EEDF has the following expression:

$$f(\varepsilon) = \epsilon^{-\frac{3}{2}}\beta_1 \exp\left(-\left(\frac{\varepsilon\beta_2}{\epsilon}\right)\right) \tag{2.16}$$

$$\beta_1 = \Gamma\left(\frac{5}{2}\right)^{\frac{3}{2}}\Gamma\left(\frac{3}{2}\right)^{-\frac{5}{2}}, \beta_2 = \Gamma\left(\frac{5}{2}\right)\Gamma\left(\frac{3}{2}\right)^{-1} \tag{2.17}$$

Where ε is the electron energy, ϵ is the mean electron energy and Γ is the incomplete gamma function. Therefore, the rate coefficient will be determined by:

$$k_f = \gamma \int_0^{\infty} \varepsilon\, \sigma_k(\varepsilon) f(\varepsilon) d\varepsilon \tag{2.18}$$

Where $\gamma = \left(\frac{2q}{m_e}\right)^{0.5}\left(\frac{c^{0.5}}{kg^{0.5}}\right)$, m_e is the electron mass (kg), ε is the energy (V), $\sigma_k(\varepsilon)$ is the collision cross section (m^2), and f is the electron energy distribution function [30].

Heavy particle reaction rate are obtained from prescribed constant reaction rate or temperature dependent reaction rate expression. The reaction rates are obtained from the rate constant expressions having the following formula:

$$R_i = \sum_i x_i N_n k_i n_i \tag{2.19}$$

Where x_i, N_n, k_i, n_i are the mole fraction, total neutral number density, rate coefficient, colliding particle number density respectively. Chemical kinetics boundary conditions encompass 7 surface reactions. The surface reactions considered are summarized in in Table. 2.2.

Transport properties are obtained based on a mixture-averaged model in which the binary Maxwell-Stefan diffusivities are computed based on the data specified for each species. The diffusivity of every species is calculated by:

$$D_i = (1 - Y_i)/(\sum_{j \neq i} \frac{X_j}{D_{ij}}) \quad (2.20)$$

Where D_i is the diffusivity of every species, Y_i is the mass fraction of the species, X_j is the mole fraction of every other species and D_{ij} is the binary diffusion coefficient which is diffusivity of one species in another species [31].

Binary diffusion coefficient is calculated based on the following formula:

$$D_{ij} = 2.66 \times 10^{-2} \sqrt{(T^3(M_i + M_j)/2 \times 10^{-3} M_i M_j)/(P_0 \sigma_i \sigma_j \Omega_D)} \quad (2.21)$$

Where M is the molecular weight of every species, T represent the temperature, σ_i is equals the characteristic length (Å) of the Lennard-Jones/Stockmayer potential, P_0 represents the pressure and $\Omega_D$is collision integral which was obtained from literature [32].

Species mobility is computed from Einstein relation:

$$\mu_i = \frac{D_i . q}{k_b . T} \quad (2.22)$$

Where, μ_i is the mobility of every species, q is the electrical charge, k_b is the Boltzmann constant and T is the species temperature, which is equal to the gas temperature.

The electron energy diffusivity and mobility are obtained based on the following relations, based on Einstein's relation from a Maxwellian EEDF:

$$\mu_\varepsilon = \frac{5}{3}\,\mu_e \;, D_\varepsilon = \mu_\varepsilon T_e \tag{2.23}$$

Where, $\mu_\varepsilon, D_\varepsilon$ are the electron energy mobility and diffusivity respectively and T_e is the electron temperature.

Mobility of helium ions is calculated based on constant values which are obtained from literature [15]. Table 2.3. represent the mobility and diffusivity of the electrons and helium ionic species. All other species transport properties are calculated based the mixture averaged model and Einstein relations.

Table 2.1- Gas Phase Chemical Kinetics

Elastic 1	$e + He \rightarrow He + e$	E
Excitation 1	$e + He \rightarrow He(2^1S) + e$	E
Excitation 2	$e + He(2^1S) \rightarrow He + e$	E
De-excitation 1	$e + He \rightarrow He(2^3S) + e$	E
De-excitation 2	$e + He(2^3S) \rightarrow He + e$	E
Ionization 1	$e + He \rightarrow He^+ + 2e$	E
Ionization 2	$e + He(2^1S) \rightarrow He^+ + 2e$	E
Ionization 3	$e + He(2^3S) \rightarrow He^+ + 2e$	A
Three-body recombination 1	$2e + He^+ \rightarrow He + e$	A
Three-body recombination 2	$2e + He^+ \rightarrow He^* + e$	A
Recombination 1	$e + He_2^+ \rightarrow He + He^*$	E
Elastic 2	$e + N_2 \rightarrow N_2 + e$	E
Ionization 4	$e + N_2 \rightarrow N_2^+ + 2e$	E
Three-body recombination 3	$2e + N_2^+ \rightarrow N_2 + e$	A
Molecular ion conversion 1	$He^+ + 2He \rightarrow He_2^+ + He$	A
Molecular conversion 1	$He(2^1S) + He \rightarrow 2He$	A
Molecular conversion 2	$He(2^3S) + 2He \rightarrow He_2^* + He$	A
Molecular ion conversion 2	$He(2^3S) + He(2^3S) \rightarrow e + He + He^+$	A
Molecular ion conversion 3	$He^+ + N_2 \rightarrow N_2^+ + He$	A
Molecular ion conversion 4	$He_2^+ + N_2 \rightarrow N_2^+ + 2He$	A
Molecular ion conversion 5	$He^+ + N_2 + He \rightarrow N_2^+ + 2He$	A
Molecular ion conversion 6	$He_2^+ + N_2 + He \rightarrow N_2^+ + 3He$	A
Molecular ion conversion 7	$He(2^3S) + N_2 \rightarrow e + He + N_2^+$	A
Molecular ion conversion 8	$He(2^1S) + N_2 \rightarrow e + He + N_2^+$	A
Molecular conversion 3	$He(2^3S) + N_2 + He \rightarrow e + 2He + N_2$	A
	E is for EEDF, A is for Arrhenius.	

Table 2.2- Surface reactions

$He(2^1S) \rightarrow He$
$He(2^3S) \rightarrow He$
$He^* \rightarrow He$
$He_2^* \rightarrow 2He$
$He^+ \rightarrow He$
$He_2^+ \rightarrow 2He$
$N_2^+ \rightarrow N_2$

Table 2.3 Transport properties.

Electron mobility	$\mathbf{2.08 \times 10^{24}/N}$
Ion mobility ($\mathbf{He^{+}}$)	$3.23 \times 10^{22}/\mathrm{N}$
Ion mobility ($\mathbf{He_2^{+}}$)	$4.88 \times 10^{22}/\mathrm{N}$

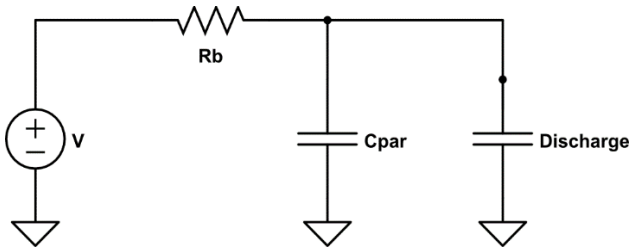

Figure 2.2. Schematics of the electrical circuit used in the simulation of the discharge (V=500, 1000 V, Rb= 1 kΩ to 30 MΩ , Cpar= 0.01 pF)

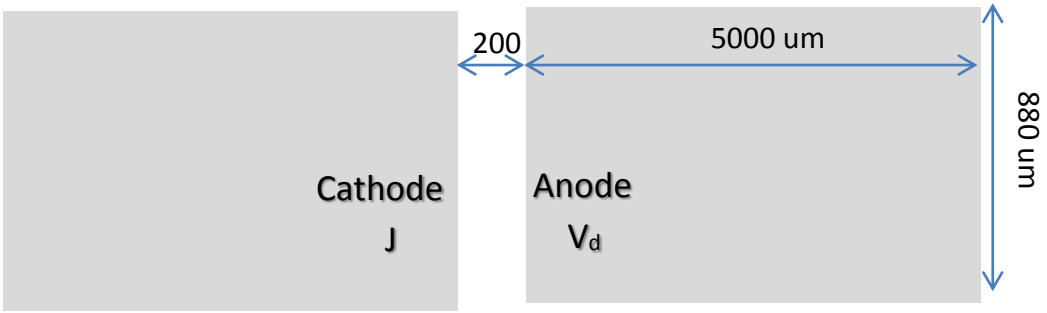

Figure 2.2. Parallel plate configuration, V_d is the discharge voltage, j is the Current density.

CHAPTER 3

ONE-DIMENSIONAL MODELING OF HIGH PRESSURE DISCHARGE

The set of governing equation was discretized on the basis of finite element method and is solved using a time dependent solver in COMSOL [30]. A non-uniform mesh was employed with denser grids present closer to the electrodes. 150 grid points were used in the simulations where the grid size ranged approximately in between 0.5 um and 2 um. One dimensional simulations of high pressure micro plasma discharge operating in the "*abnormal" glow mode* was conducted. Effect of operating pressure on the discharge was investigated and the influence of gas heating on the plasma characteristics was quantified.

Conjugate heat transfer analysis was performed and was found to provide better predictions compared to the conventional Dirichlet boundary conditions. Since the conjugate heat transfer analysis adds up numerical expenses to the simulations, an analytical approach has been conducted to solve the conduction heat transfer in electrodes in order to obtain the temperature distribution of electrodes and use the electrode tip temperature as boundary temperature.

For the conjugate heat transfer analysis, the electrodes length is set to be 5000 um, which has a cylindrical shape, and the radius is fixed at 440 um resulting in a cross sectional area of 0.006 cm^2. A schematic of the computational domain in presented in Figure 3.1. The electrode material is

chosen to be molybdenum to be consistent with published experimental data [17]. Those experimental data are used for model validation. The effect of different electrodes materials on the discharge characteristics has also been investigated. Electrode cross sectional area of ~0.006 cm^2 was prescribed for the discharge current calculation. In one dimensional simulation the electrode cross section area is required to calculate the discharge current from the current density values.

3.1. Time stepping scheme

The different time scales in plasma discharges expands over a very large range. Electron transport takes place in less than a pico second, neutral transport and reaction requires less than 100 nano seconds whereas neutral gas temperature transport needs seconds (Figure 3.2). Therefore in order to accurately capture the different physical phenomena, simulation must be conducted with very small time step size. But this constrains the simulation time as the slowly evolving neutral gas temperature will not reach steady state conditions easily with the smallest of time step. Hence, a dynamic time step size control is critical for efficient simulation.

All the simulations have been conducted by employing a dynamic time stepping algorithm. The plasma discharge partial differential equations are vastly stiff, to overcome the stiffness of the problem and to be able to handle the dynamic time stepping schemes a second order "*back differentiation formula"* formula is used. Figure 3.3 shows the time step size temporal evolution where

this evolution helps to capture all plasma characteristics in shortest possible computational time. Gas temperature is the last parameter to attain steady state condition, which indicates that at the time gas temperature reaches steady state condition all the other plasma characteristics has already attained that. Conduction heat transfer reaches steady state at even slower pace than gas temperature, therefore the steady state conditions have been determined for gas temperature and solid phase temperature. It is shown that when CHT is included whole system reaches a steady state condition in less than 6 seconds (Figure 3.4). Cases without CHT analysis tend to reach steady state condition in less than a second; therefore, time marching has been chosen accordingly to avoid any extra numerical expenses.

3.2. Pressure dependence of the discharge

Pressure has a strong effect on plasma discharge characteristics, since based on the ideal gas law it will have a direct effect on the neutral number density. Neutral number density is the determining factor of some of the basic discharge characteristics e.g. the ion and electron number density.

Breakdown voltage is determined by pressure and gap distance, pressure would affect the neutral number density value and the gap distance affects the collisionality of the discharge. As gap distance grows larger the collisionality increases thereby increasing the breakdown voltage. Based on this concept, Paschen’s law was introduced which states that: the breakdown voltage of a

plasma is dictated by the pressure x distance; “*pd*” scaling - breakdown and steady state discharge voltage is the same for identical “*pd*” values [14].

Pressure affects the discharge current directly. An increase in pressure results in an increase in discharge current. This is due to fact that increase in pressure will cause the higher concentration of neutral atoms and molecules to get ionized and thereby increase the overall charged species concentration in the system. Figure 3.5 depicts the charges species number density for different operating pressures. It is evident that increase in pressure will increase the number densities. With more species available in the system the current density will increase proportionally. Furthermore because of inverse relation of diffusivity with neutral number density, diffusivity decreases with increase pressure. As a result the positive column is more easily formed and apparent at higher operating pressure [34].

Figure 3.6 depicts the voltage current characteristics curve for three different pressures, where discharge current is found to increase almost linearly with pressure. At low pressure discharge current is known to scale with effective pressure [34], whereas high pressure discharges due to higher gas heating the discharge will not scale with effective pressure alone since gas temperature plays an important role in the rarefaction of the gas.

3.3. Conjugate heat transfer analysis

High pressure micro plasma discharge experiences high rates of gas heating. This is due to the fact that even at these small sizes of the plasma the

heat diffusion is significantly lower than that of low pressure plasma discharge at the same time higher electron density results in higher ion joule heating which is one of the main sources of heat generation. CHT analysis has been conducted to capture the temperature predictions more accurately and at the same time predict the changes in the electrode temperature. Figure 3.7 depicts the spatial temperature distribution and compares the predictions from the Dirichlet boundary condition and CHT analysis. There is almost 300 K peak temperature difference between two cases. This huge difference in gas temperature distribution has vast effects on other plasma characteristics such as electron density. Electron density peak increases with higher gas temperature, since the higher gas temperature increases the reduced electric field (E/N) which in turn increases the ionization rates which is the main source of electron density. Besides this the peak electron number density also shifts toward the right increasing the cathode sheath size. The reason for increasing the cathode sheath is that the gas temperature increase rarifies the gas and hence the reduced electric field (E/N) shifts towards the location of the peak gas temperature which increases the heavy particle reactions rate that are responsible for ionization inside the plasma discharge (Figure 3.8). Within the CHT analysis, free convection on the electrodes has been analyzed and has been found not affect the plasma discharge temperature distribution significantly.

Figure 3.9 depicts the spatial temperature distribution within the entire domain that encompasses both the solid and gas phase. The linearity of the conduction heat transfer shows the steady state condition in electrodes. The

base temperature of the electrodes is set to be 298 K which is room temperature. It is possible to use a Robin boundary condition (free convection over the electrode base), but since the free convection heat transfer coefficient is small and will not change the base temperature that much, it is not considered to avoid additional numerical expenses.

The novelty of conjugate heat transfer approach is not only capturing the more realistic temperature distribution, but also it lets the discharge to dictate the temperature of the electrodes. With constant boundary simulation, anode and cathode temperature had the same values and was dictating the temperature of the discharge (which can be a good approximation depending on which value is chosen for the boundary condition). According to the ion joule heating spatial distribution (Figure 3.10), the IJH around the cathode has higher values so the cathode temperature should be higher than the anode temperature, which is shown by CHT analysis

The CHT analysis will only be effective for plasma conditions where there is significant gas heating present. As such discharges operating in "*normal"* and "*abnormal"* regimes will be strongly affected by the CHT component of the model unlike "*subnormal*" glow discharges where the gas temperature rise is typically insignificant, but as gas heating increases the difference between CHT results and Dirichlet results increases (Figure 3.11). Simulation results were also compared with experimental results. CHT analysis results showed better agreement with experiments than those obtained from Dirichlet boundary

conditions. The comparison between predictions and measurements are presented in Figure 3.12.

3.4. Effects of electrodes material on the discharge

Electrode's material is a determining factor on the discharge characteristics but Dirichlet boundary condition simulations does not consider the electrodes thermal properties while the CHT analysis includes electrodes conductivity, density and heat capacity. These properties (Table 3.1 and Table 3.2 [18]) change the temperature distribution significantly. Figure 3.13 depicts the temperature distribution with three different electrodes (Steel, Platinum-Rhodium, and Molybdenum). It is evident that with increase in thermal diffusivity gas temperature decreases, while the Dirichlet boundary temperature cannot capture the temperature difference since it does not include the variation in the thermo-physical properties of the electrode material. This difference in gas temperature also affects all other discharge characteristics, as explained in previous section of this chapter. The electron number density peak increases with decrease in thermal diffusivity of the electrode material (Figure 3.14). The cathode sheath thickness increases for materials with less thermal diffusivity. Different electrode materials were effective on the VI characteristics curve as well as other plasma characteristics. Materials with less thermal diffusivity tend to have higher discharge voltage. As gas temperature increases, the difference between discharge voltages increases (Figure 3.15). Electric field dependence on the electrode material is not only limited to thermal properties, but thermal properties

of the electrodes are also an effective factor on the spatial electric field distribution. Figure 3.16 depicts the spatial electric field distribution for these three different electrodes where difference in the electric field is due to the effects of the material on the gas temperature. For materials with less thermal diffusivity, where gas temperature is higher, electric field reversal effect is observed. Electric field reversal happens when the electron diffusion current is higher than the total current ($\frac{J_{e,diff}}{J} \geq 1$). Total current at the anode sheath is carried by electrons mostly and electron current can be divided to drift and diffusion current part. With higher gas temperature the electron diffusion current will increase significantly, while the total current density over the whole domain and also for different materials remains nearly the same (Figure 3.17-18). Electron diffusion current depends on the number density gradients and the electron diffusivity. Electron diffusivity is proportional to electron temperature and electron temperature increases with increase in gas temperature. Hence with higher gas temperatures the electron diffusivity will increase which will result in higher electron diffusion current. As the diffusion current increases at the same direction of total current, the electric field direction changes to sustain the total current. Therefore in regions where $\frac{J_{e,diff}}{J} \geq 1$ the electric field changes from negative to positive and electric field reversal occurs (Figure 3.19). This reversal in electric field directly affects the drift current.

Conjugate heat transfer analysis was not only important in predicting a more accurate gas temperature distribution, but it also helps the simulation to

consider the effects of electrode materials on gas temperature and plasma characteristics.

3.5. Temporally Varying Temperature Boundary Condition

Conjugate heat transfer analysis adds numerical expenses to the system since additional domain and physics is added to the model. So the need for an alternative solution was sensed, to avoid these extra simulation and numerical expenses. In addition to numerical expenses, the steady state conditions can be reached in less than 1 second with an analytical solution for heat transfer in electrodes.

Heat transfer in electrodes of the discharge resembles one of the classical conduction heat transfer problems - one-dimensional heat transfer in a slab with changing boundary heat flux [17]. For the purpose of obtaining a solution for this case the boundaries are defined as:

$$q'' = f(T_g, t), \qquad T(\delta) = T_0. \tag{3.1}$$

Where, δ is the penetration depth, which is a point in a semi-infinite slab where the following conditions hold true:

$$T(\delta, 0) = T_0, \qquad \frac{\partial T(\delta, t)}{\partial x} = 0 \tag{3.2}$$

Where T_0 is the ambient temperature and is set to be 298 K, penetration depth denotes the regions beyond which the varying boundary does not affect the temperature distribution inside the slab. An expression for δ can be determined which is as follows:

$$\delta = \sqrt{12\alpha t} \tag{3.3}$$

Where, t refers to the solution time (s) and α is heat diffusivity of the electrodes.

The final solution for finite flat plate (same as the plasma electrodes) is a two-step solution which is dictated by the relationship of the penetration depth and the length of the electrodes. The solution for the temperature profile based on these relationships are as follows:

For $\delta \leq L$

$$T(x,t) = \frac{q_w^{"}\delta}{3k}\left(1 - \frac{x}{\delta}\right)^3 + T_0 \tag{3.4}$$

For $\delta > L$

$$T(t) = \frac{q_w^{"}L}{k}\left(1 - 0.814\exp\left(-\frac{12\alpha t}{5L^2}\right)\right) \tag{3.5}$$

Using this boundary condition will cause instability and divergence in the simulation, since the temporal evolution of heat flux happens in micro seconds and heat transfer module cannot follow those large changes at small time scales. In order to circumvent this limitation, heat flux should change at a moderate step by step fashion so that the heat transfer module could compensate inward heat flux to the electrodes. For this purpose, a stepping method was applied to decompose the heat flux into discrete values. This decomposition method had the following expressions:

$$q_{new}^{"} = e^{\frac{floor[\log(q^{"}\times Sf)]}{Sf}} \tag{3.6}$$

Where the "*floor*" operator eliminate converts a real number to an integer. In essence this floor operator is spitting out the power of heat flux going into the boundary. "*sf"* is responsible for broadening the range of integers coming out of the "*floor"* operator, and when normalized by "*sf"* provides more data points and a smoother time varying profile of heat flux. Figure 3.20 depicts the stepping method applied to simple logarithmic function. Increase in the "*sf*" results in more data points taken into calculation which results in more accurate results.

Since this method may decrease the accuracy of temperature distribution predictions. To avoid this reduction in accuracy, the stepping function (sf) was set to have different values and the results were compared to CHT temperature prediction results. Figure 3.21 depicts the spatial temperature predictions with four different stepping functions compared to CHT results. For Sf=2, the results are a little offset but for Sf =10, 100, 1000 the results are found to be in a good agreement with the CHT results. Only 30 K difference between predictions is observed. The Sf is considered to be 1000 in order to have the most accurate results. As shown in Figure 3.22, numerical expenses were reduced by 30 percent with use of the analytical boundary condition instead of solving conducting the CHT analysis.

Temperature distributions were compared to experimental results [16], and final simulation results does not lie completely within the error bars of the experimental results (Figure 3.23). A possible source to the observed discrepancy could be the presence of some external gas flow which is not taken into account in the current simulations. The cathode temperature predictions are

also compared against experimental measurements. This comparison (Figure 3.24) shows a good agreement to experimental results. The experimental cathode temperature measurements are done for a feed gas having a mixture composition of 99.9% He and 0.1 % N_2.

The choice of secondary electron emission coefficient on the voltage current characteristics was also investigated. Secondary electron emission coefficient represents the fraction of electrons emitted from the electrode surface due to ion bombardments. The predicted voltage-current characteristic is sensitive to the secondary electron emission coefficient. Higher secondary electron emission from the cathode decreases the discharge voltage as less electric field is required for sustaining the electron production due to the higher concentration of electrons generated from the cathode surface. When comparing the predicted voltage-current curve to the measured one it was found that a secondary electron emission coefficient $\gamma = 0.15$ provided the best agreement (Figure 3.25) for both the CHT and temporally varying boundary condition approach.

Figure 3.26 depicts a comparison between different approaches to temperature boundary conditions. Surprisingly the experimental results had a better agreement with the predictions where the Dirichlet boundary condition for the gas temperature was prescribed. However this agreement does not make this particular approach more reliable since the boundary temperature can be set arbitrarily to obtain the best agreement. A pre-chosen boundary temperature can

change the results significantly while the CHT analysis and analytical boundary condition approach is free from providing a biased result.

Table 3.1. Thermal properties of the different electrode materials [18]

Material	Melting Point (K)	Density (kg/m^3)	Specific Heat (J/kg K)	Conductivity (W/m K)	Diffusivity m^2/s
Steel	1670	7900	477	14.9	3.95×10^{-6}
Pt-Rh	1800	16630	162	47.0	17.4×10^{-6}
Mo	2894	10240	251	138	53.6×10^{-6}

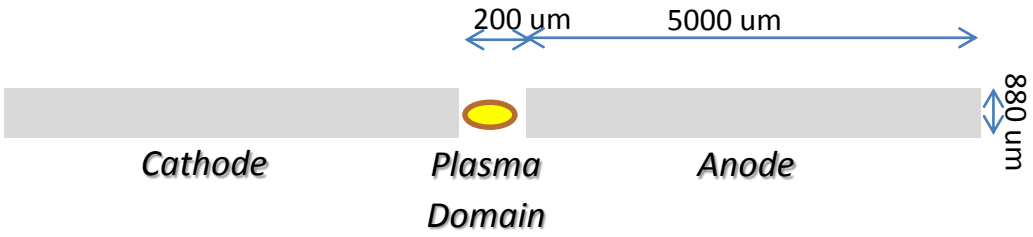

Figure 3.1. Schematic of the computational domain.

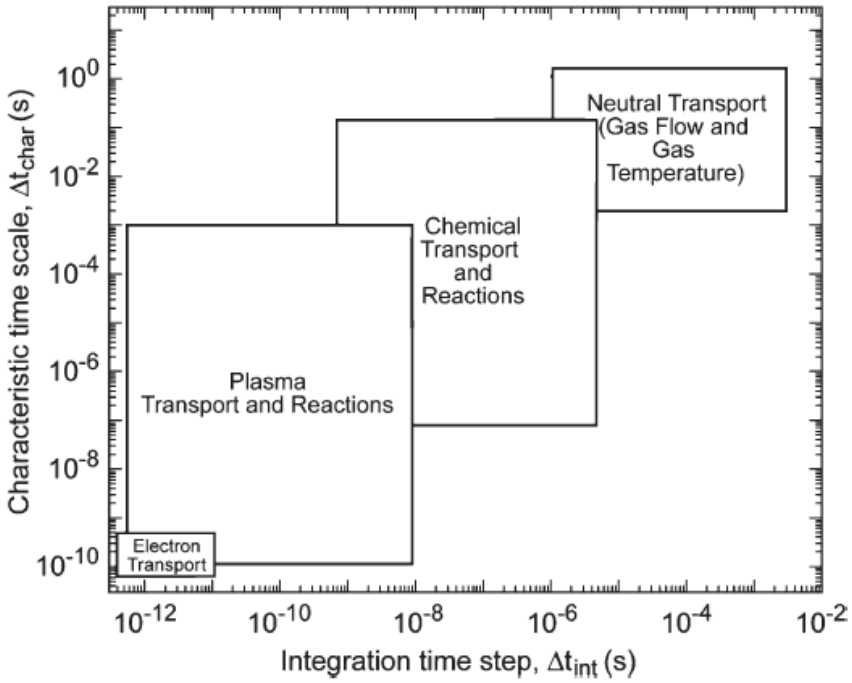

Figure 3.2. Time step size needed for solving different characteristics of plasma [33].

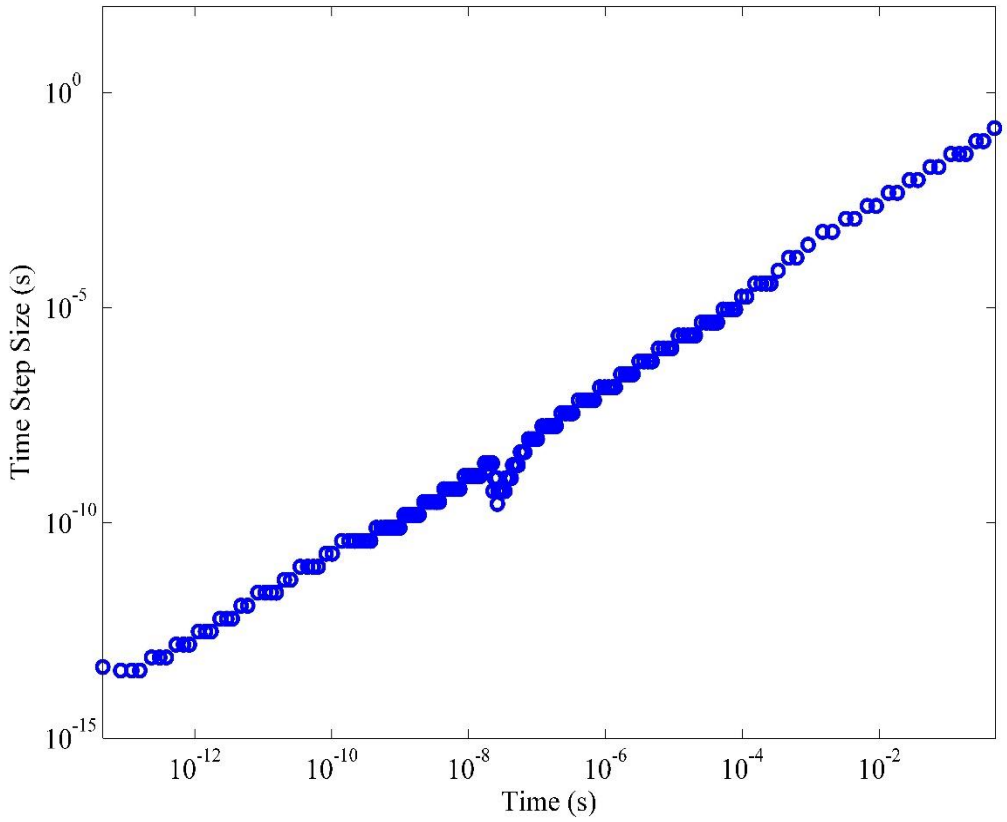

Figure 3.3. Temporal evolution of time step size, V_d= 160 V, I_d= 5 mA, R_b= KΩ C_{par}=0.01 pF

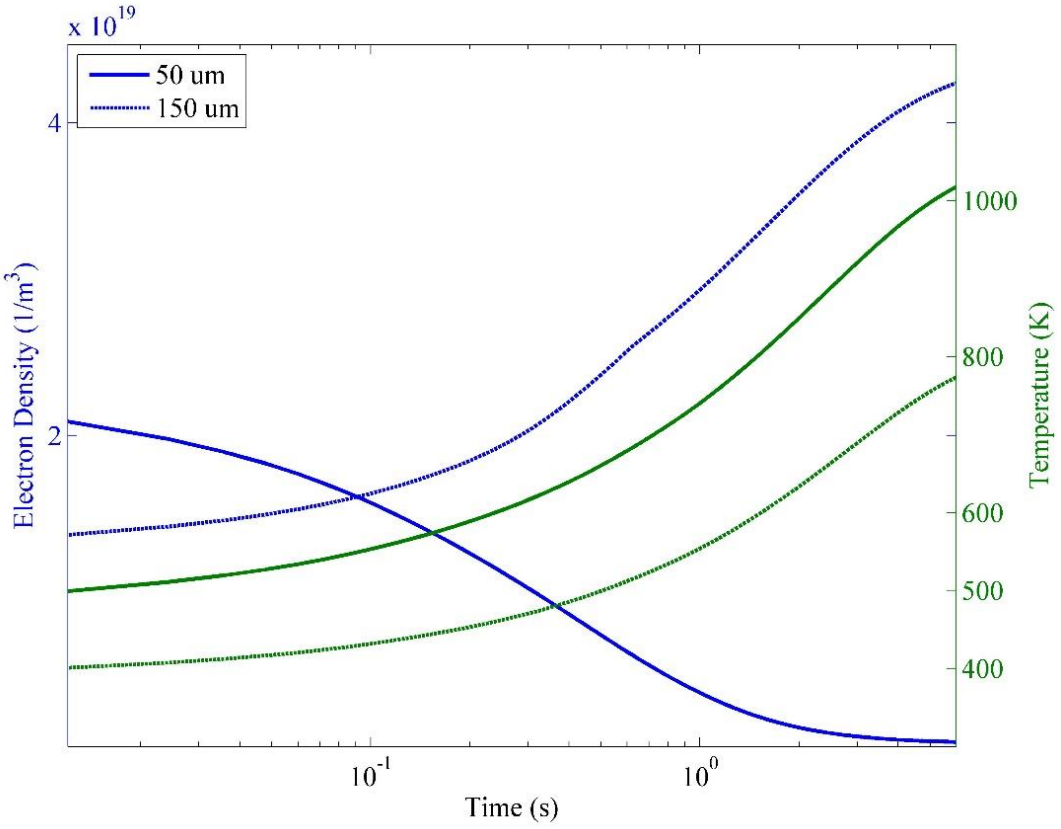

Figure 3.4. Gas temperature and electron number density temporal evolution at different axial location, V_d= 160 V, I_d= 5 mA.

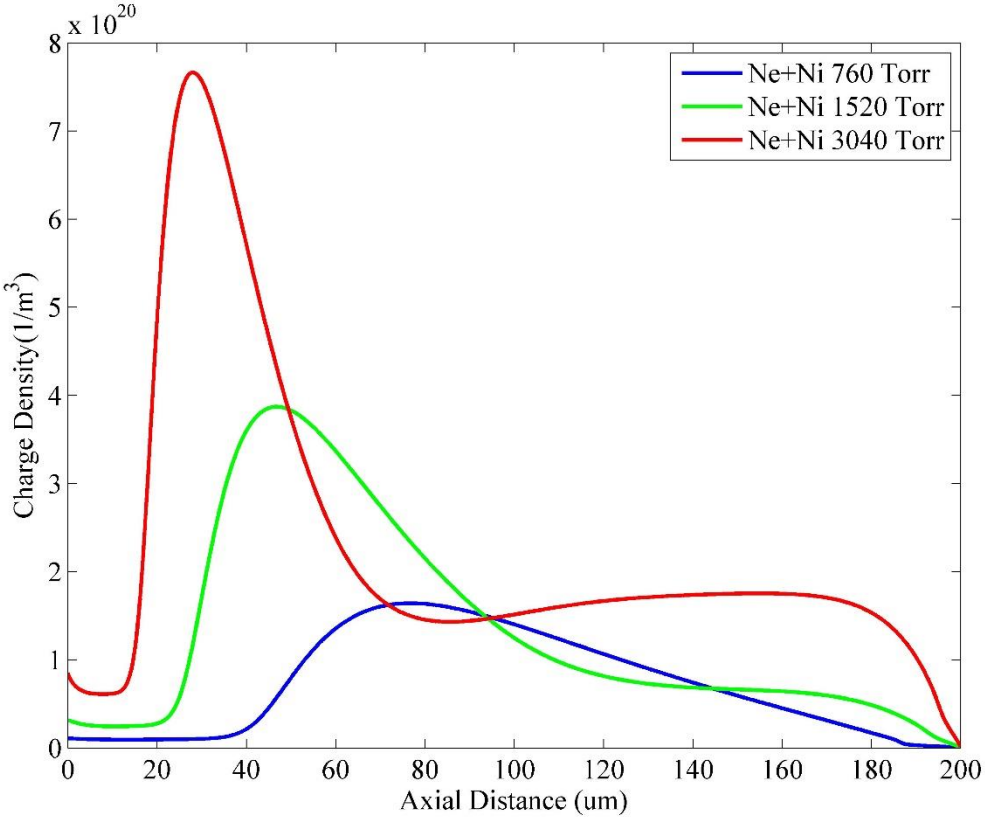

Figure 3.5. Charged density spatial distribution for different pressures V_d=200 V.

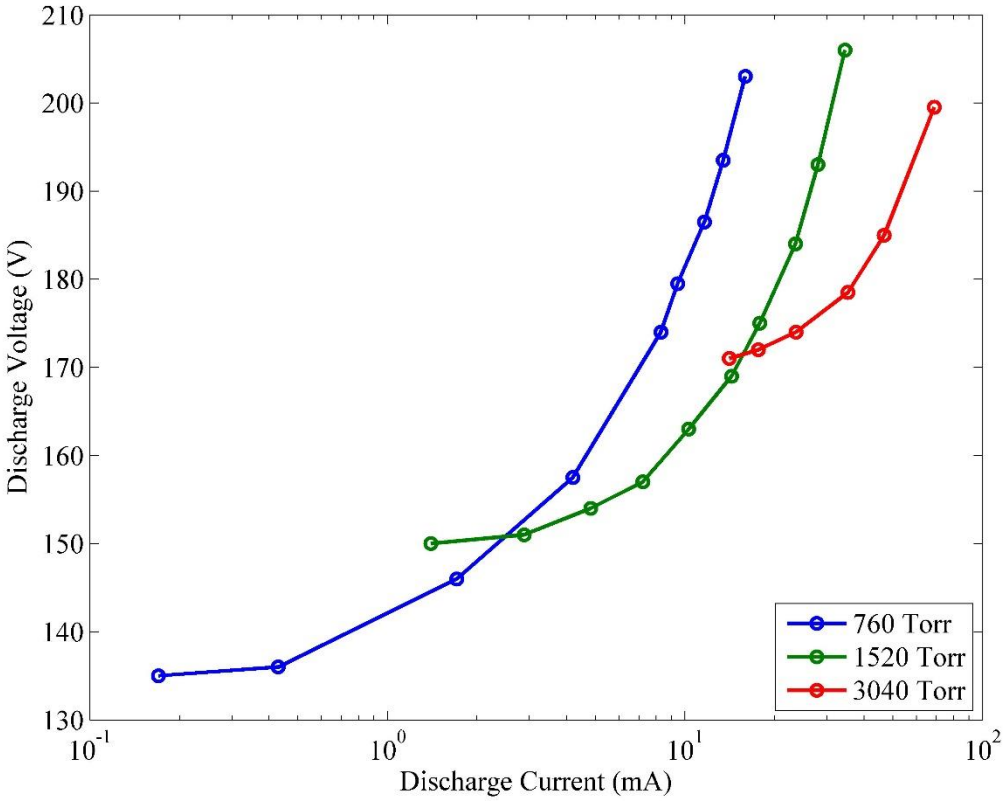

Figure 3.6. Voltage current characteristics curve, pressure comparison.

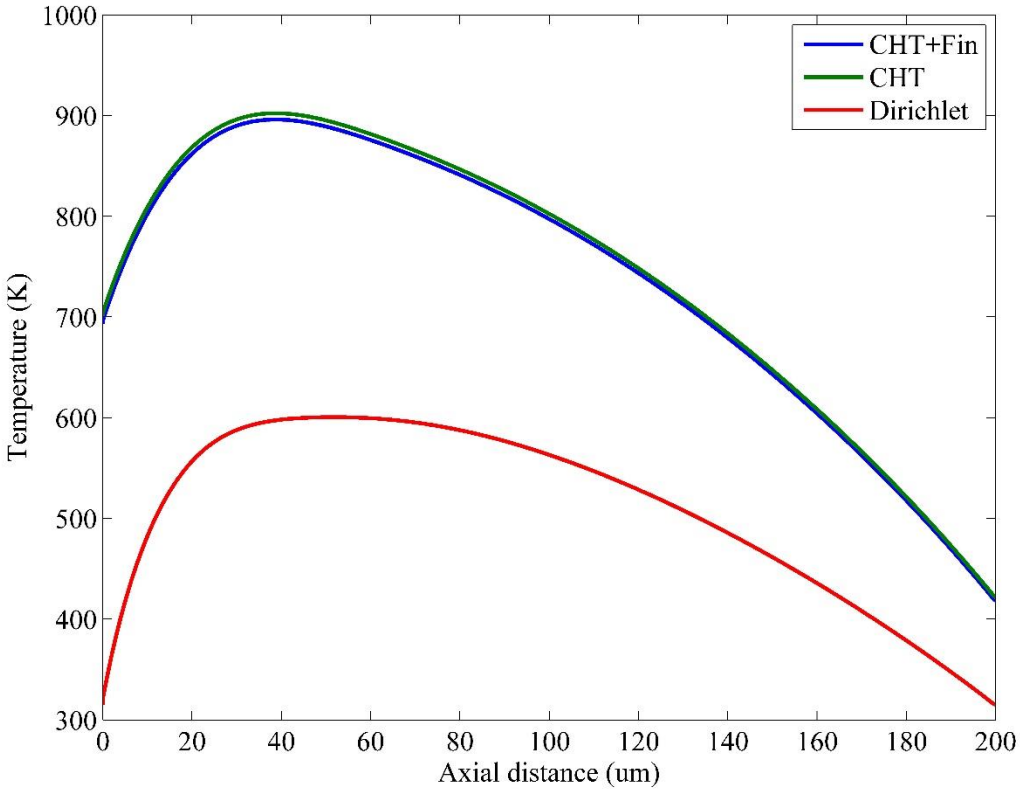

Figure 3.7. Comparison of spatial temperature distribution for different gas temperature boundary conditions

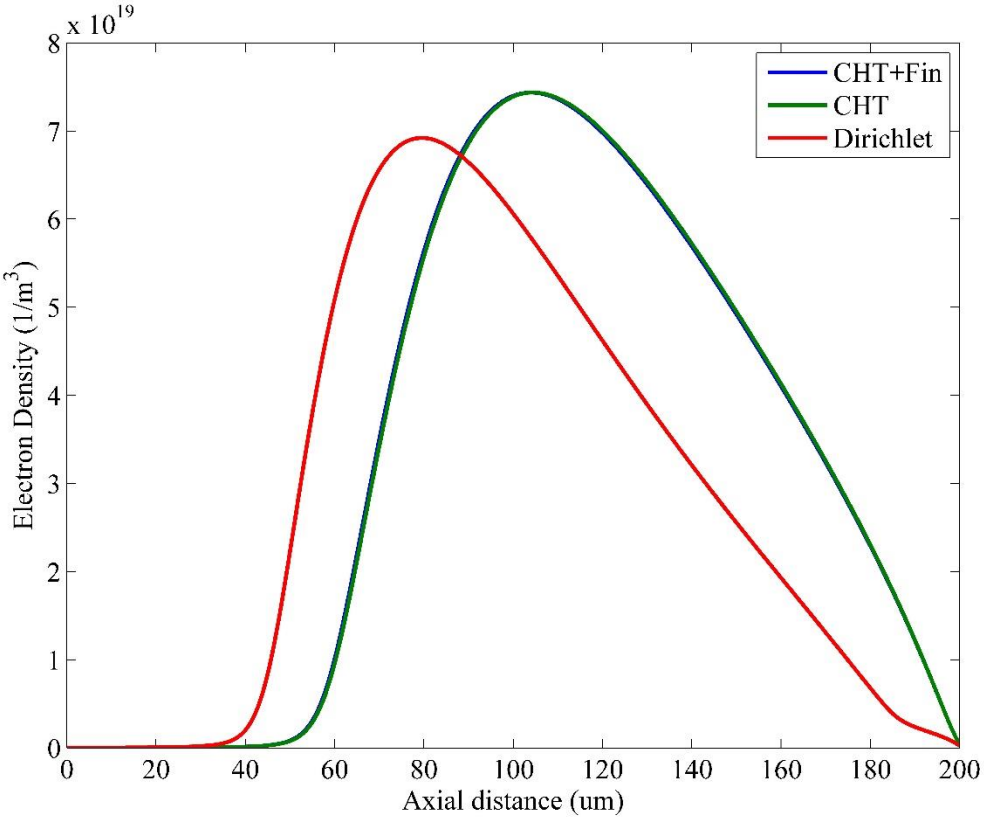

Figure 3.8. Comparison of spatial electron density distribution for different gas temperature boundary conditions

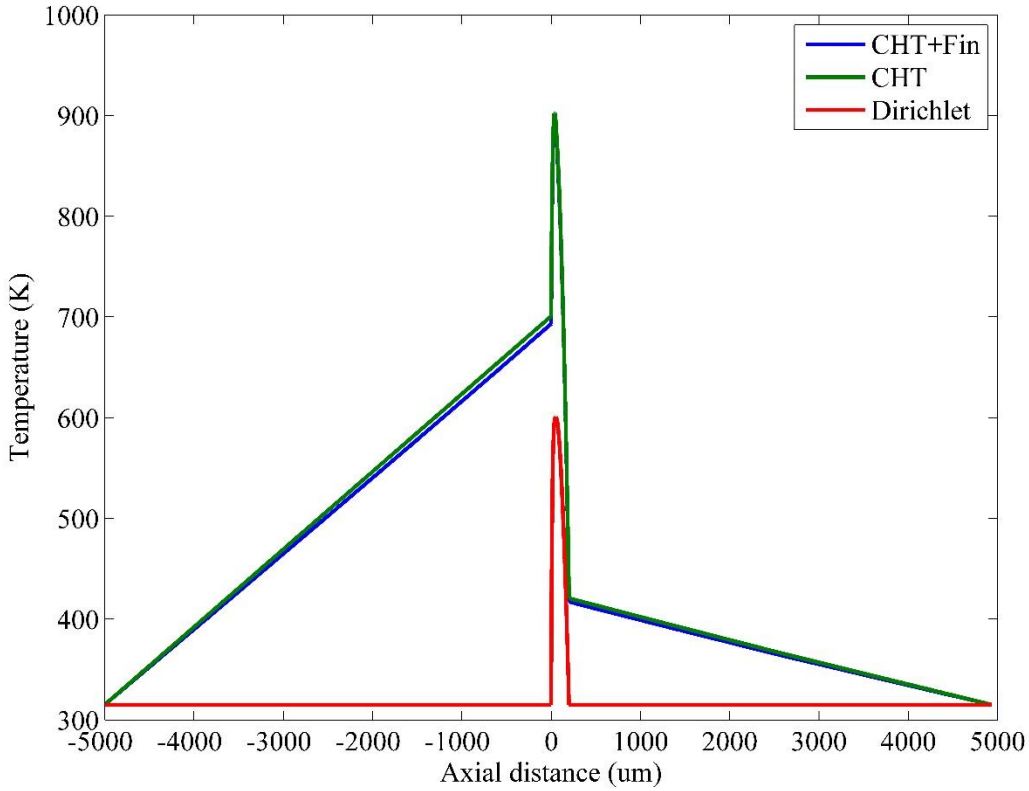

Figure 3.9. Comparison of spatial temperature distribution over the electrodes, for different approaches to the gas temperature boundary.

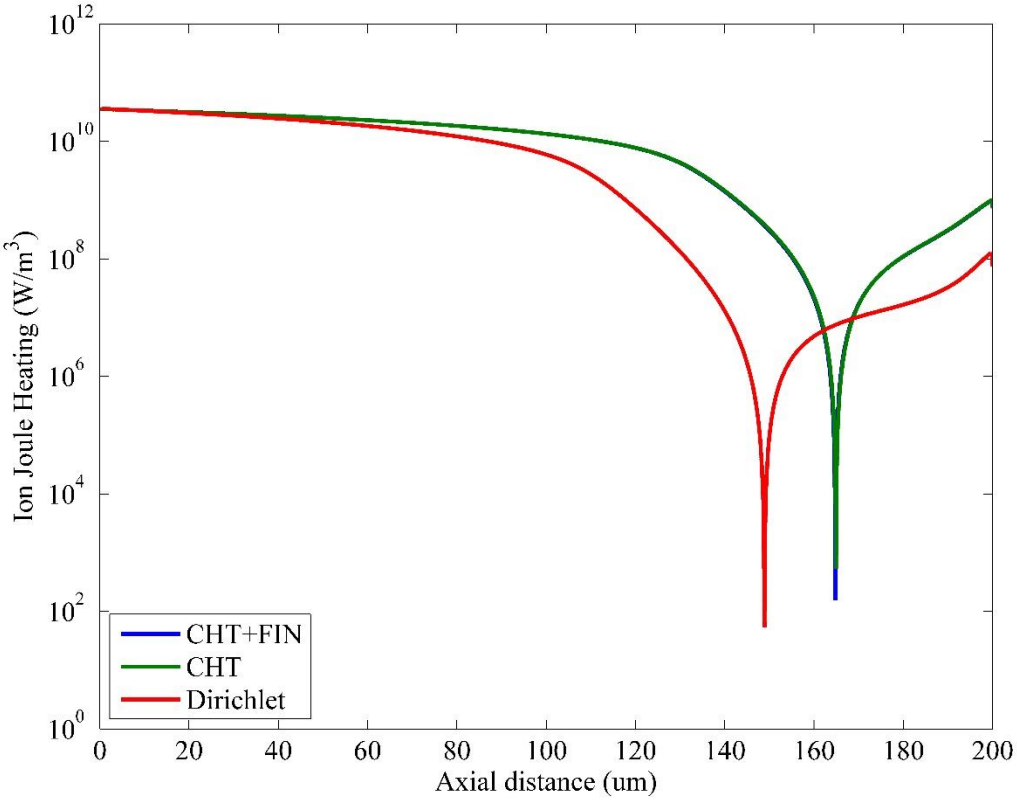

Figure 3.10. Spatial distribution of ion joule heating for different approaches to the temperature boundary.

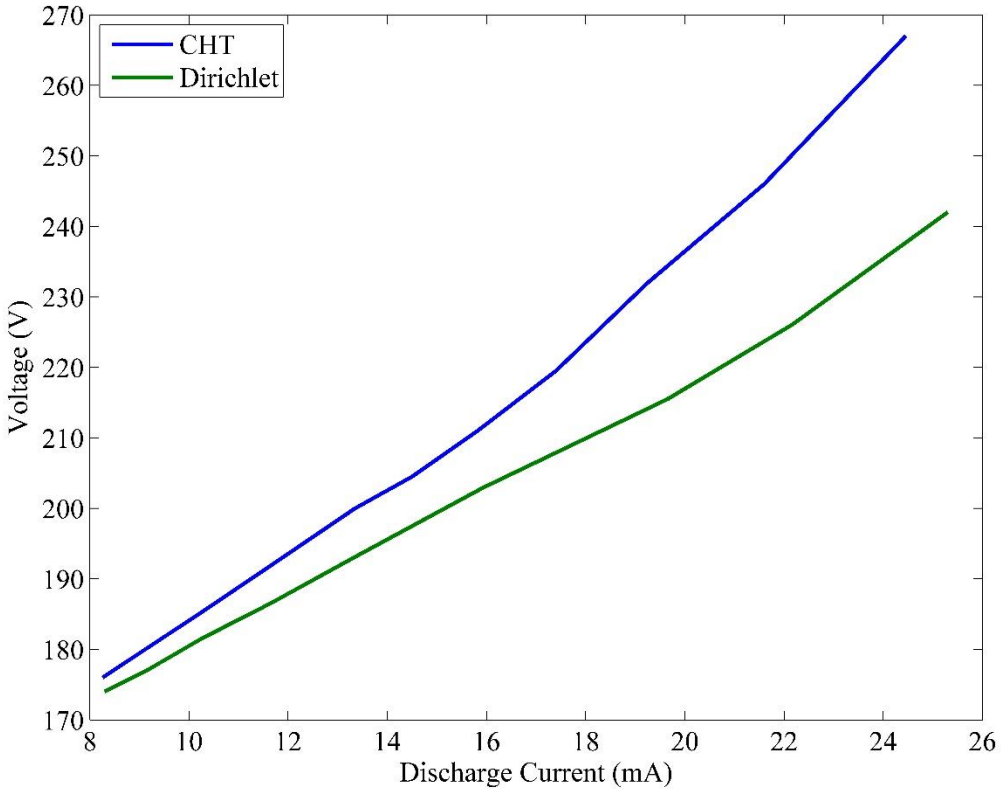

Figure 3.11. Comparison between CHT and Dirichlet boundary condition imposed VI characteristics curve predictions.

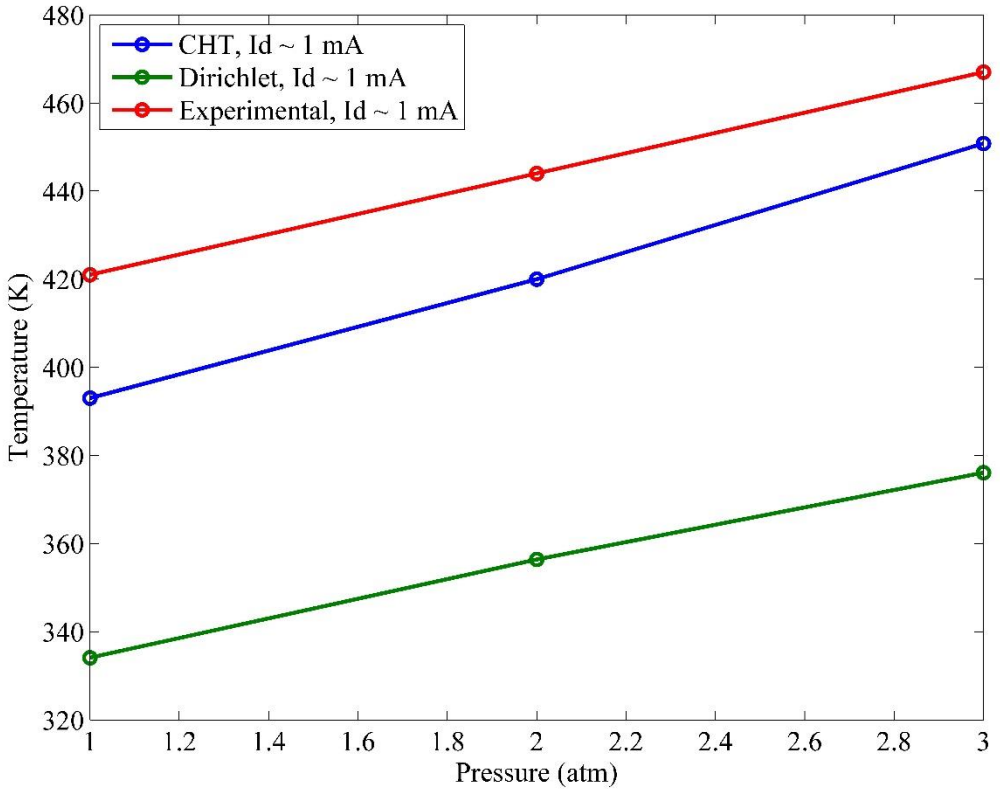

Figure 3.12. Peak temperature comparison with experimental peak temperature, experimental results courtesy: Dr David Staack, Texas A&M. T_0= 300 K.

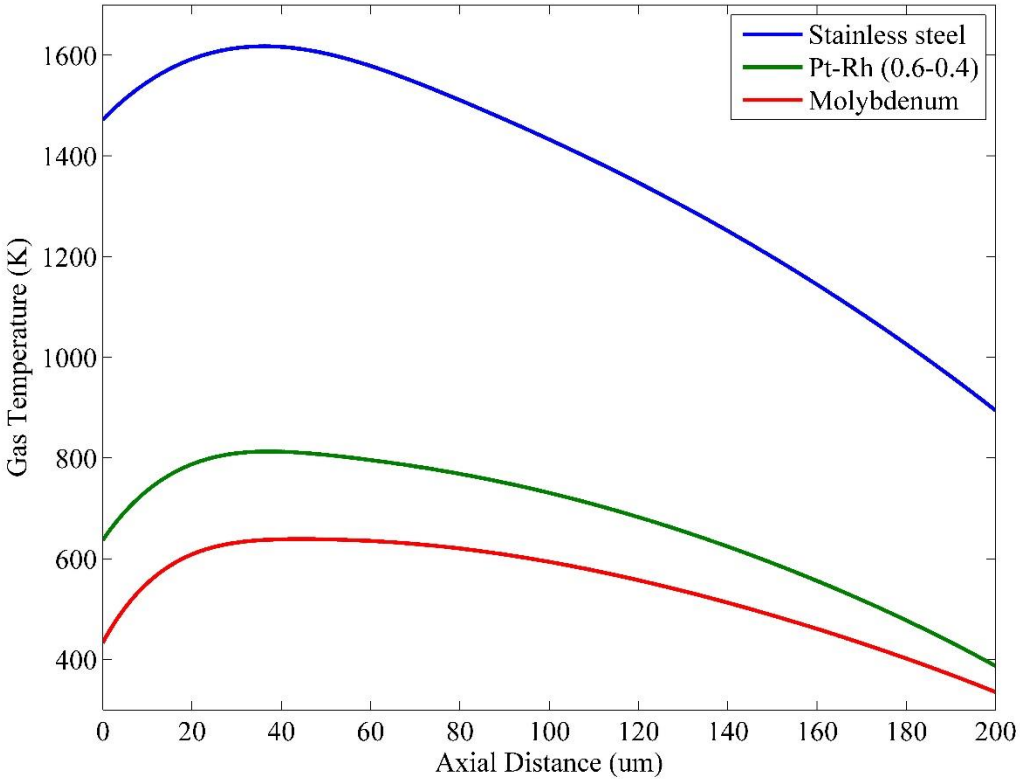

Figure 3.13. Temperature distribution for different electrode materials.

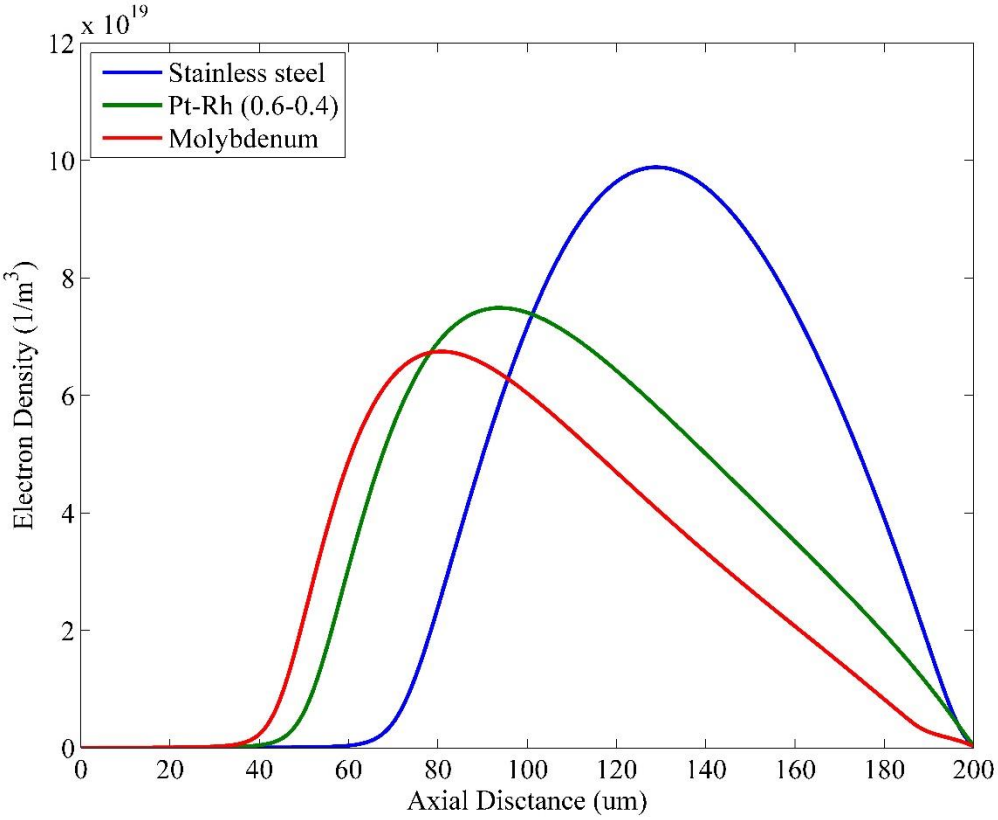

Figure 3.14. Spatial electron density distribution for different electrode materials.

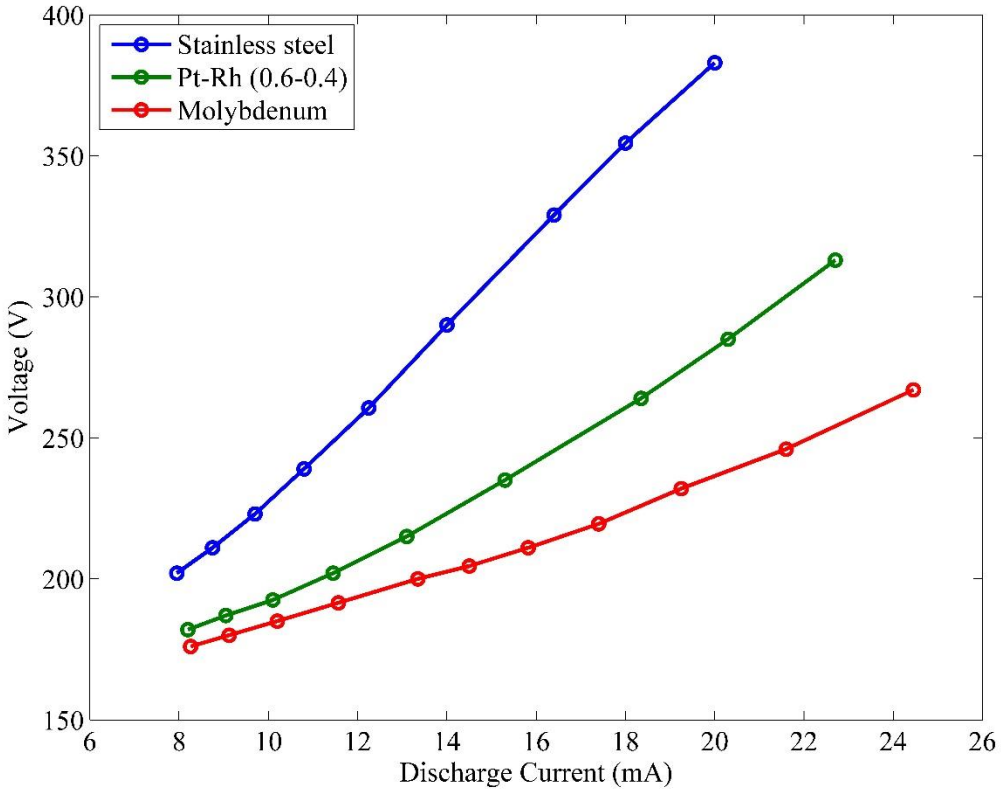

Figure 3.15. VI for different electrode materials.

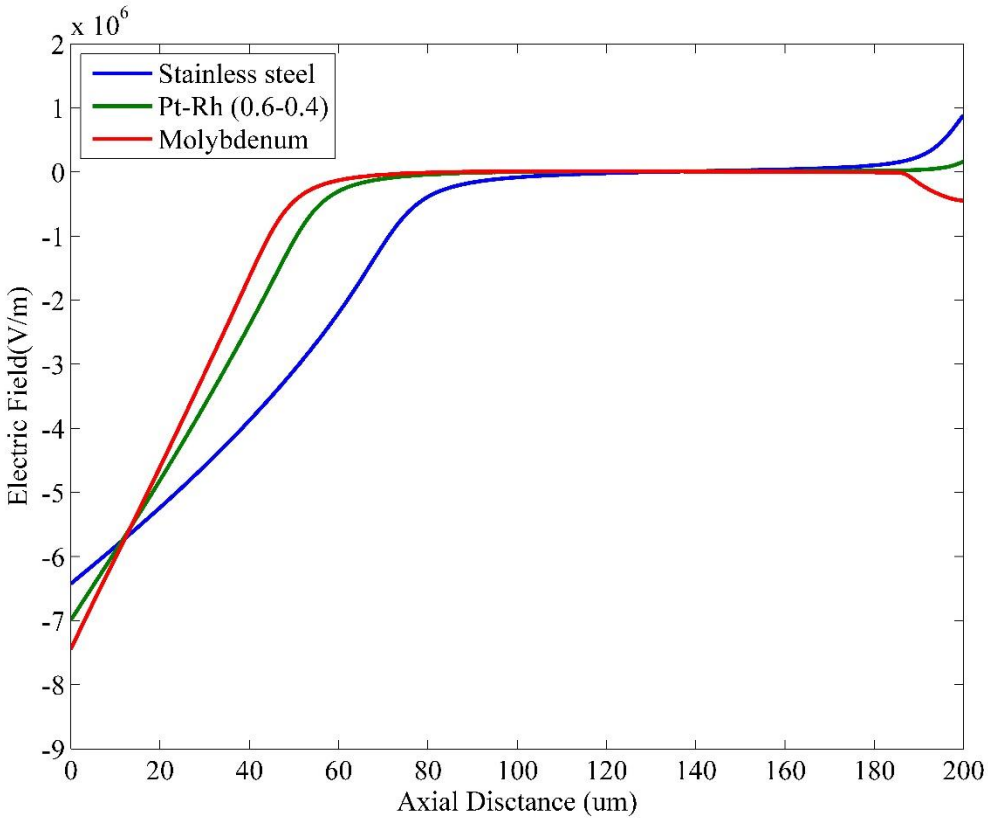

Figure 3.16. Electric field spatial distribution for different electrode materials.

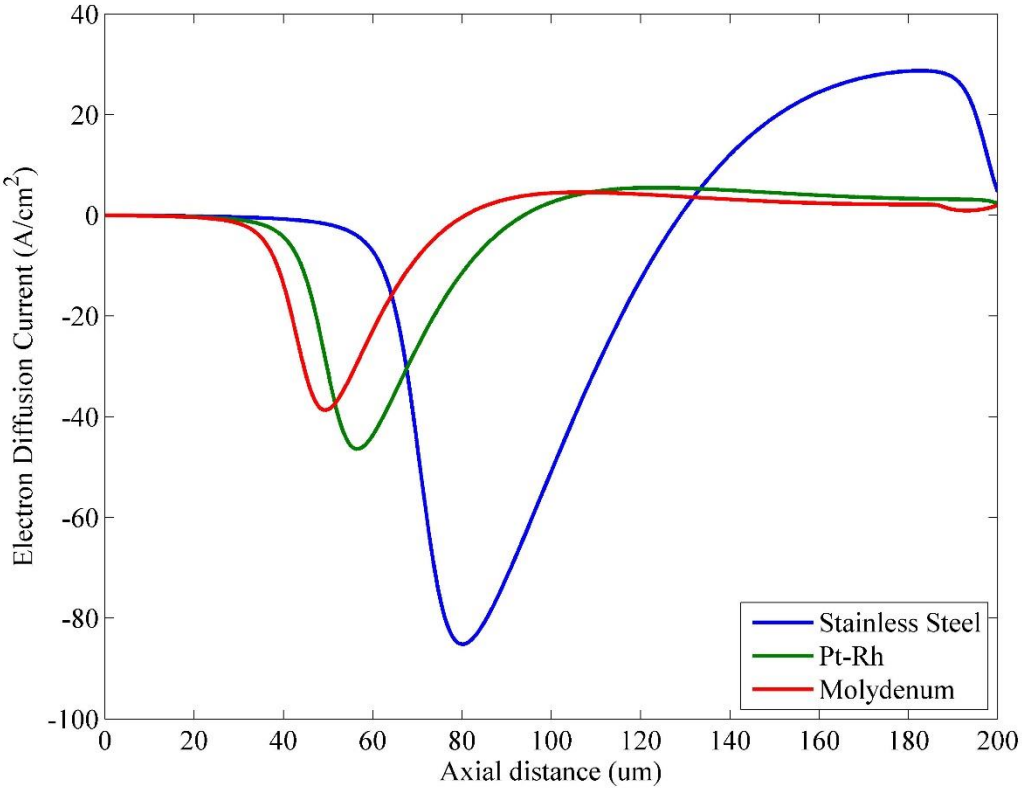

Figure 3.17. Electron diffusion current spatial distribution for different electrode materials.

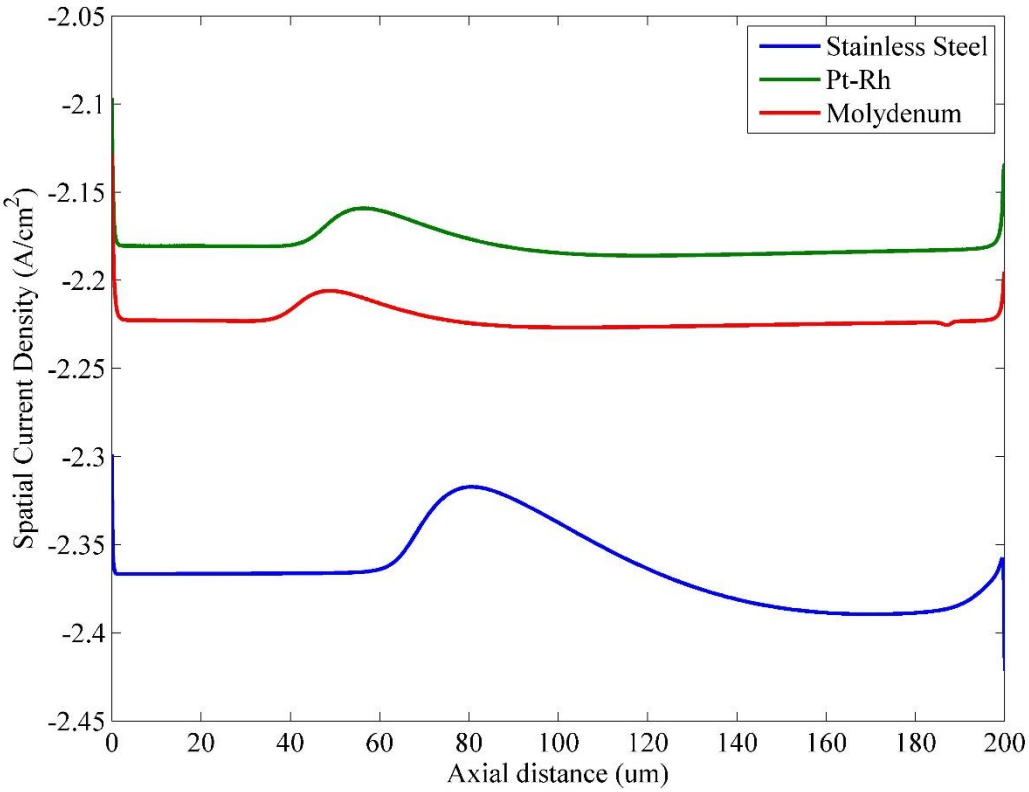

Figure 3.18. Total current density spatial distribution for different electrode materials.

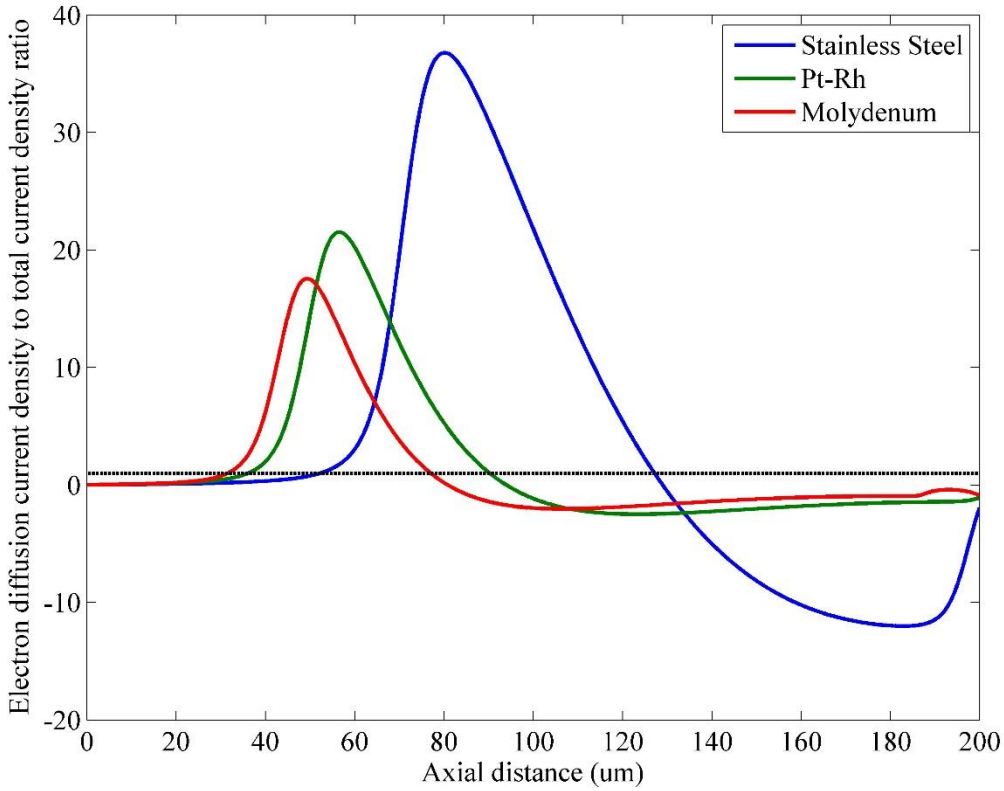

Figure 3.19. $\frac{J_{e,diff}}{J} \geq 1$ spatial distribution for different electrode materials.

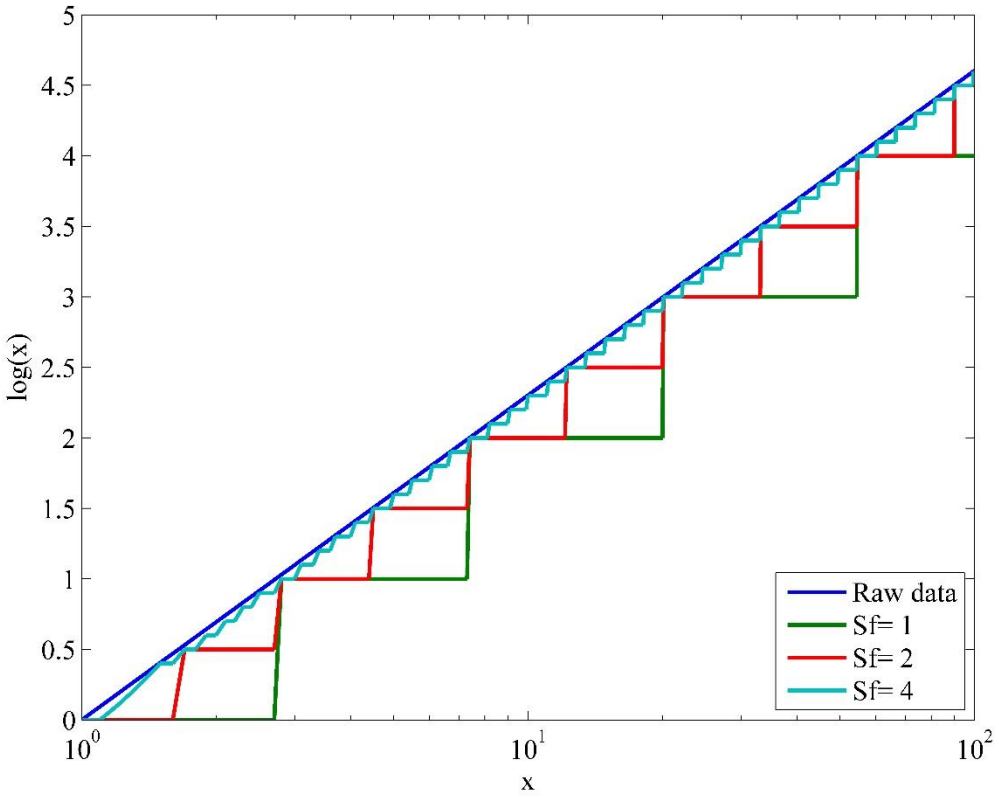

Figure 3.20. Stepping method applied to f=log (x) with increasing SF accuracy increase.

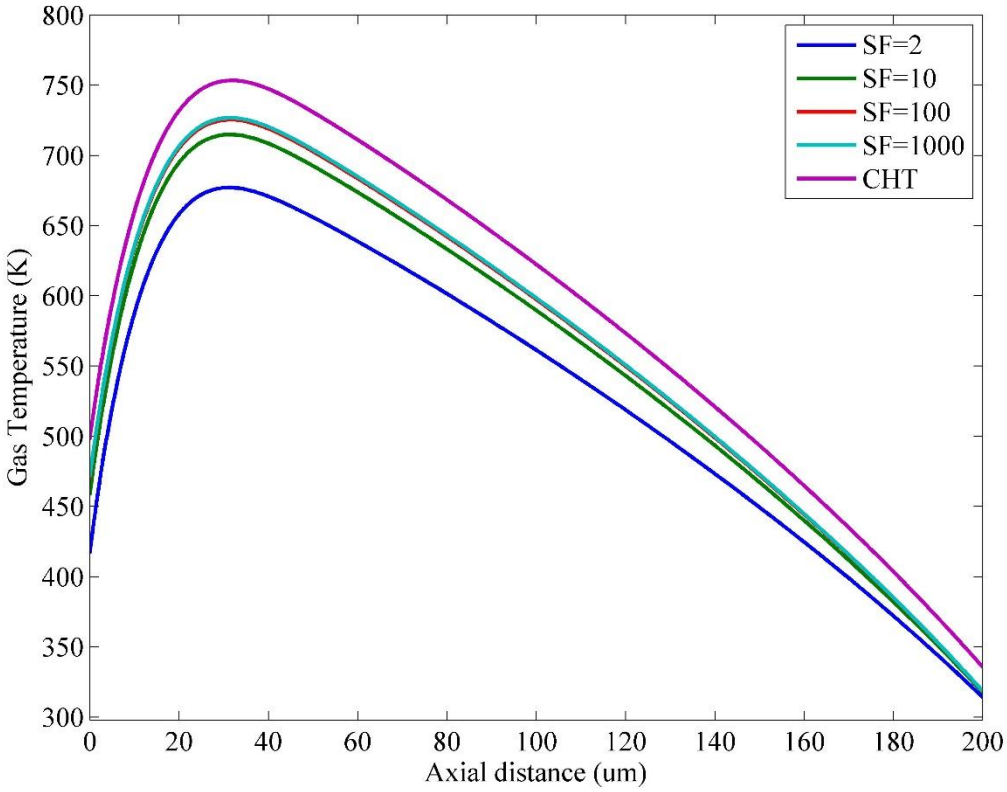

Figure 3.21. Spatial temperature distribution with the applied BC compared to Dirichlet and CHT analysis.

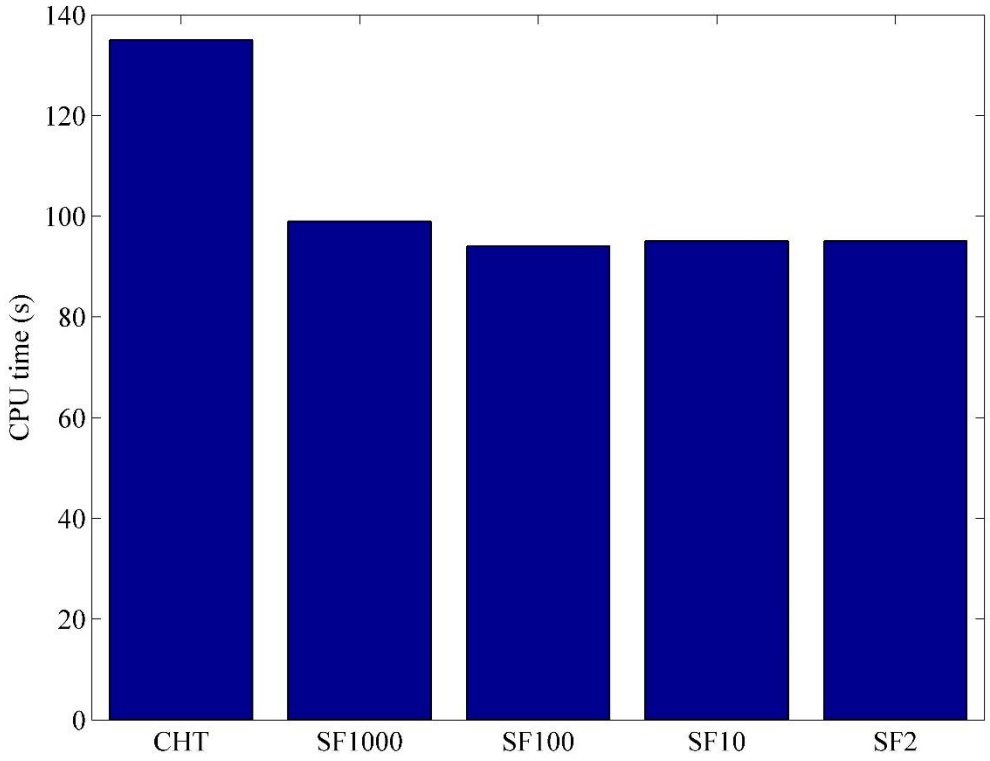

Figure 3.22. CPU time for different approaches to temperature boundary, it is evident that the analytical boundary condition is more efficient. The analytical boundary decrease the computational time 30 %.

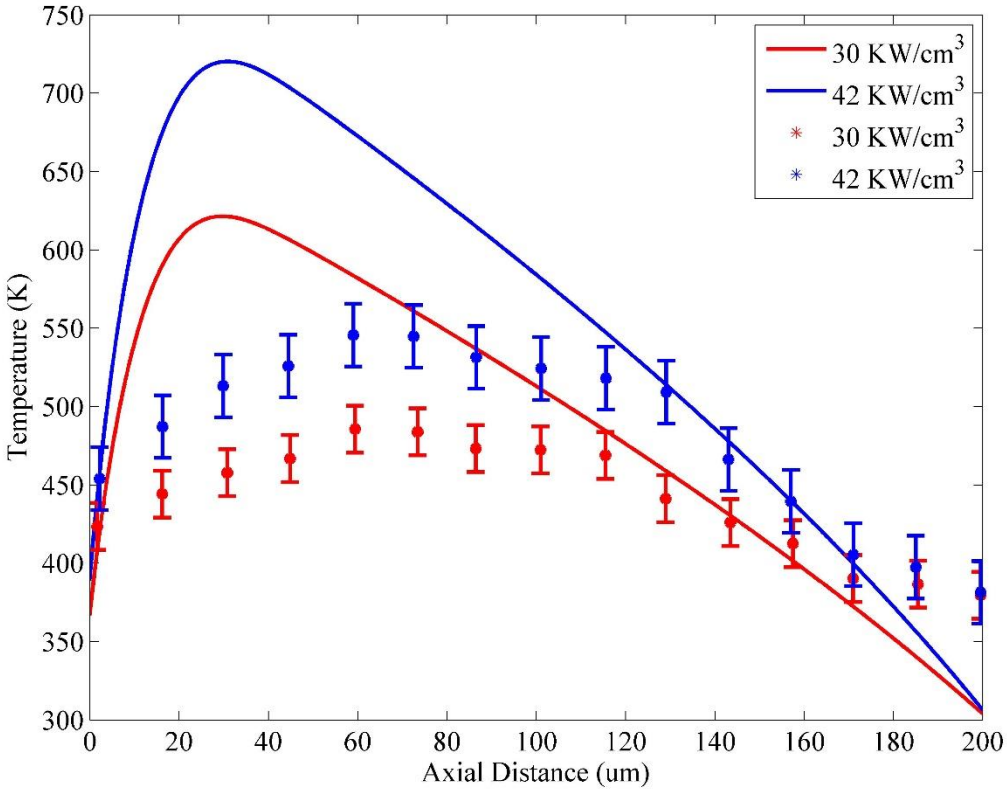

Figure 3.23. Comparison of predicted spatial temperature distribution against experimental measurements. The simulations are conducted with the temporally evolving temperature conditions. The experimental measurements are that of [17].

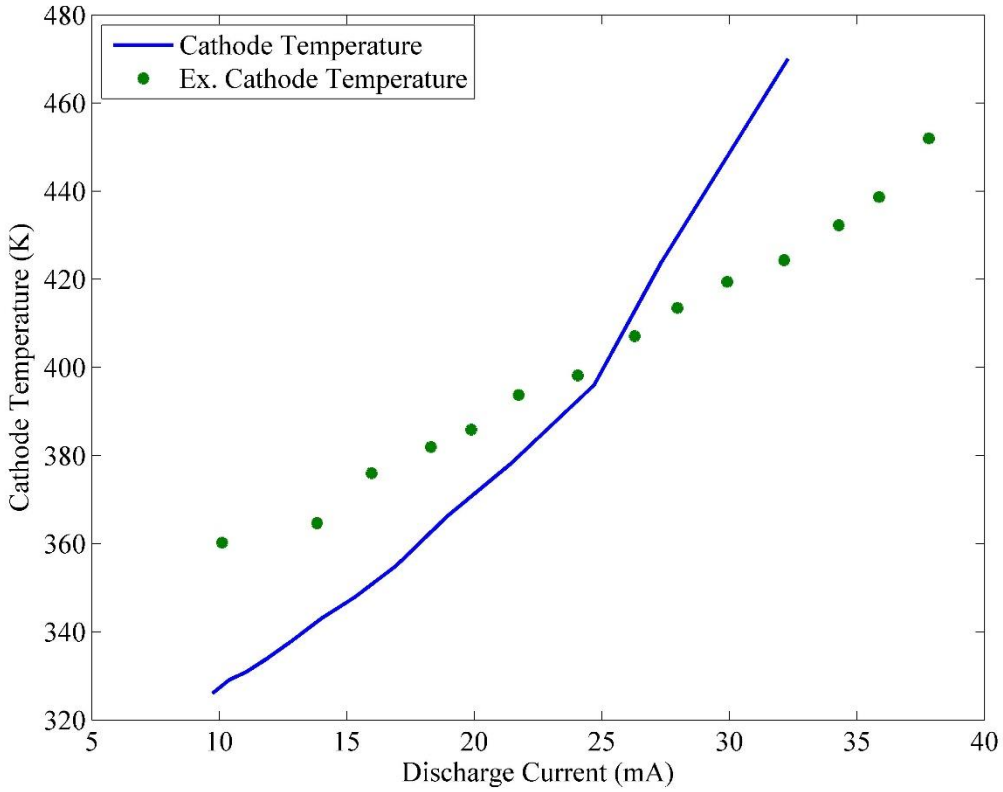

Figure 3.24. Comparison of predicted cathode temperature with the temporally evolving temperature boundary conditions against experimental measurements.

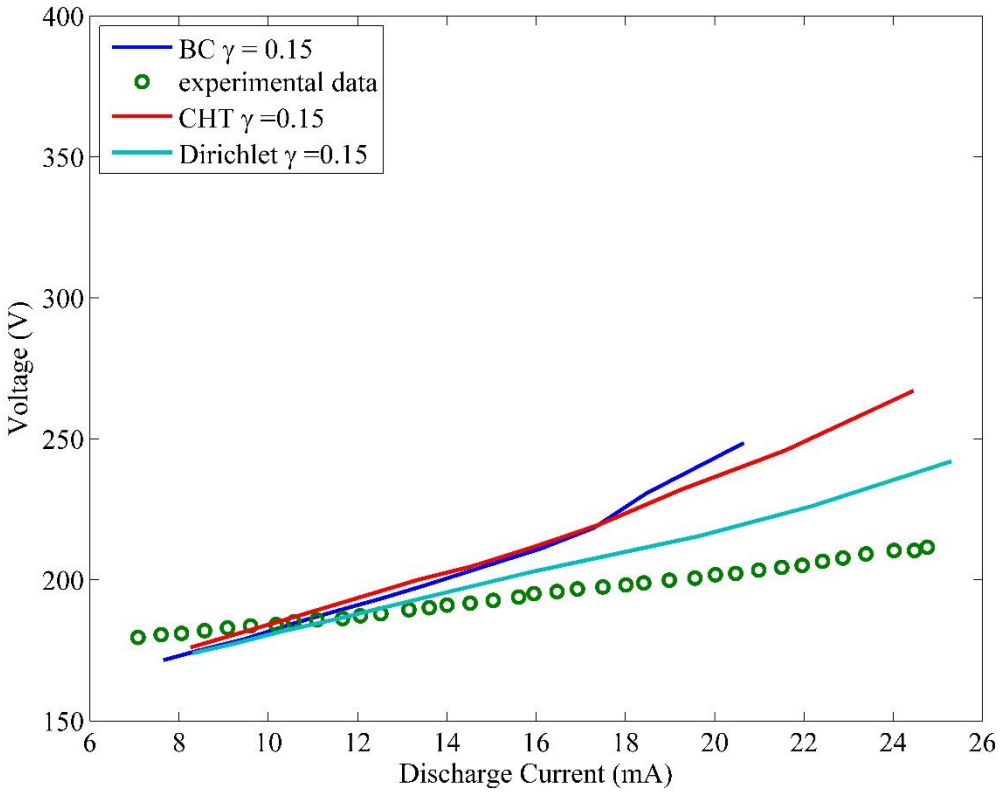

Figure 3.25. VI curve, comparison between the approaches in resolving the gas phase temperature simulation

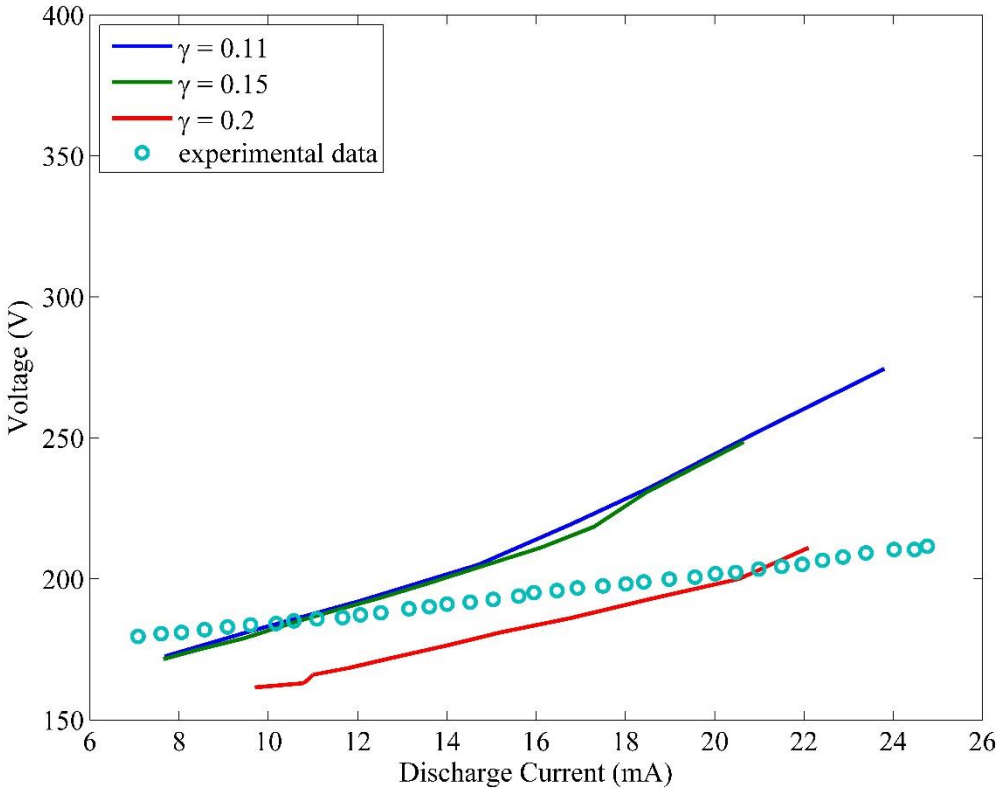

Figure 3.26. VI curve, parametric study on secondary emission

CHAPTER 4

TWO-DIMENSIONAL SIMULATION OF HIGH PRESSURE DISCHARGE

In this chapter results from the two-dimensional axisymmetric simulations are discussed and summarized. Our one dimensional model was unable to include the radial losses hence unable to provide any information about radial distribution of the discharge. A severe limitation of the one dimensional model is that it cannot capture the "*normal*" glow characteristics because the electrodes are treated as a point location with the assumption that the discharge is uniform in the radial direction. But a "*normal"* glow discharge is known have a two dimensional structure and therefore assuming a uniform radial distribution is incorrect. In a VI curve the "*normal"* glow mode has a flat profile where the discharge voltage remains constant for increasing discharge current. The discharge current in the "*normal"* glow increases only due to the increase of the discharge size in the radial direction with a constant current density. Therefore a one-dimensional model will predict the "*normal"* glow region as a turning point from "*subnormal*" glow discharge to "*abnormal*" discharge.

The effect of pressure and gas heating on the normal glow discharge has been studied employing a two-dimensional axisymmetric model. It was found that at high pressure, normal glow discharge and the discharge voltage scales with pressure and gas temperature. Effects of conjugate heat transfer is analyzed on

the normal glow discharge, where the gas heating increased due to the increase in total current.

4.1. Geometry and Modeling

Figure 4.1 shows the schematic of the simulation geometry. The domain represents a cylindrical configuration with an axisymmetric boundary at the center line, a dielectric wall boundary as the cylinder walls and two electrodes at the top and bottom where the top boundary is the anode and the bottom boundary is the cathode. The inter-electrode separation is set to be 200 um, Reaction kinetics are the same as one dimensional model. The grid in the axial and radial directions were set to be 150 and 300 respectively.

Due to the introduction of the Dielectric walls an additional boundary condition had to be introduced which had the following expression:

$$\frac{\partial \rho_s}{\partial t} = n.J_i + n.J_e, \quad where\ -n.D = \rho_s \tag{4.1}$$

Where, ρ_s is the charge density and D is the surface charge density. Also the temperature boundary for the dielectric wall and electrodes cylinder wall were set to be a free convection type where the wall thickness is 1 um.

4.2. “*Normal*” Glow Characteristics

The evolution of normal glow discharge is depicted in Figure 4.2 - 4.5, 4.8-4.11 where it is evident that with higher total currents the discharge covers larger area of the electrode. The electron density contours and ion current density contours are shown where electron density and ion current density gradually covers the cathode area until the cathode area is completely covered with the discharge. This increase in the discharge size takes place with a constant current density. Afterwards when the entire electrode area is covered an increase in total current occurs due to the increase in current density only. As it is shown in the electron density and ion density contours, the peak electron and ion number density remains essentially constant in the “*normal”* glow range. The constant value of peak electron number density is the reason for constant current density. As a consequence the electric field and all other plasma characteristics remain constant as well. This suggests that the volumetric gas heating does not change during the “*normal”* glow discharge since the major source of gas heating is the ion joule heating and enthalpy change of heavy particle reactions.

The radial distribution of the current density for different discharge currents are presented in Figure 4.7. It shows that radial current density has its maximum at the center line of the discharge, with increasing discharge area this maximum front expands in the radial direction while the magnitude of the maximum value remains the same. This occurs till the cathode is completely covered with the discharge. The area under the radial current density profiles represent the total current which increases during normal glow while the current

density itself remains constant (Figure 4.8). The "*normal"* glow regime was found to be operating in the discharge current range of 0.15 mA - 1 mA beyond which the transition to an "*abnormal*" glow occurs.

4.3. Effects of pressure on normal glow discharge

As pressure increases, based on ideal gas law, neutral number density increases which also hinders diffusive transport. Since the cathode area remains the same an increase in pressure results in a compression of the discharge directly translating to larger discharge current range for "*normal"* glow operation mode Figures 4.12- 4.19 depict the electron density evolution for 2 atm and 4 atm normal glow discharges. "*Normal*" glow current density at higher pressures were higher than the atmospheric "*normal"* glow current density

Figure 4.20, 2.21 depicts the radial current density evolution of the normal glow discharge for 2 and 4 atm, which followed the same trend as the 1 atm discharge. The only difference is that the "*normal"* glow current density and the range of the "*normal*" glow both increase with pressure.

4.4 VI characteristics curve

Increase in pressure results in an increase in the discharge voltage due to the fact that neutral number density scales with pressure. An increase in the neutral density reduces the E/N ratio. As a result to sustain the discharge the electric field needs to increase to maintain the same E/N ratio to increase the electric field in the system the discharge voltage therefore increases. Voltage

current characteristics curve has been depicted in Figure 4.22, where increase in the discharge voltage and normal glow with increasing pressure is shown.

Normal glow is known to scale with pressure where discharge voltage, current density etc scales with pressure squared. This is the case for macro-scale low pressure normal glow discharges, where the effects of gas heating is negligible. Figure 4.23 depicts the pressure scaling of the normal glow discharge at high pressure conditions. As it is evident in the case of high pressure micro plasma discharge, the voltage scaling phenomena does not hold true. The main difference in these two types of discharge is the significant gas heating of high pressure micro plasma discharge which implies that gas temperature should play an important role in this scaling

Only factor that includes effects of temperature and pressure together is the density of the neutral gas. Density scaling has been applied to discharge voltage and Figure 4.24 depicts the density scaled VI. Based on this in high pressure micro plasma discharge, discharge voltage scales with density squared.

$$V^* = V \times \left(\frac{P_0 \times T_2}{P_2 \times T_0}\right)^2 \tag{4.2}$$

4.5. Conjugate heat transfer analysis

Gas heating per volume in normal glow mode remains constant because of constant values of electric field, reaction rates and current density. Total amount of gas heating increases by increases in discharge area. Figure 4.25

depicts the total radial gas heating evolution over the cathode (cathode radius is 250 um), it is evident that the peak value of gas heating remains constant but increases radially during the "*normal"* glow discharge operation. Even though the value of heat generation per unit volume remains constant the increase in the volume of the discharge has the potential to increase the gas temperature at higher discharge currents in the "*normal*" glow operation. This makes it crucial to have a more detailed look at gas temperature predictions Conjugate heat transfer simulations were conducted with increased cathode radius of 2500 um to maintain the "*normal*" glow condition at higher discharge currents, in order to have better perspective on the gas temperature rise. Electrodes length is assumed to be 10000 um, in which a two-dimensional heat diffusion equation has been solved. Electrode furthest length-wise boundary is set to be at 298 K (room temperature) and radial walls of electrodes and dielectric wall are assumed to follow an external free convection boundary condition:

$$-k.\nabla T = h(T - T_{\infty}) \tag{4.3}$$

Where, $h = h_{air}(L, U_{\infty}, T_{\infty}, P_0)$ (4.4)

For the ambient condition the heat transfer coefficient is set to be $15\ \frac{W}{m^2.K}$.

Most previous experiments are performed on larger cathodes areas (usually pin-plate configurations), in which at later stages of normal glow discharge gas heating turned out to be an important factor [36].

To include the effects of conjugate heat transfer, a heat conduction solver has been added to the model which is connected to plasma domain by a heat

continuity boundary condition. All the simulations of Dirichlet boundary condition are performed by using T=298 K, which is a good approximation for starting points of normal glow mode temperature distribution. But at later stages of normal glow discharge, because of higher gas heating this boundary temperature does not represent the actual boundary condition of the discharge.

Axial gas temperature prediction of conjugate heat transfer analysis and Dirichlet boundary condition analysis show a minimum of 30 K difference at the anode where the leas gas heating is happening, maximum difference happens at the edge of cathode sheet where there is nearly 80 K difference between predictions of these two methods (Figure 4.26). This difference is happening because of the fact that including the conjugate heat transfer analysis in simulation lets the electrode boundaries temperature to be determined by the amount of gas heating inside the plasma domain, while applying the Dirichlet boundary conditions forces a temperature distribution in the domain which is determined by a combination of Iso-thermal temperature boundary as well as the heat generation. It is therefore important to apply the conjugate heat transfer analysis to the model to avoid the effects of constant temperature boundary on the discharge.

Peak gas temperature predictions are depicted in Figure 4.27, in which it is evident that the peak gas temperature rises at higher total discharge current and difference between gas temperature predictions of CHT and Dirichlet boundary condition increases. The Dirichlet boundary condition imposes a strong cooling effect on the discharge and artificially suppresses the increase in the gas

temperature. This cooling effect increases with larger sized electrodes sizes. To avoid this artificial effect conjugate heat transfer analysis is essential to obtain better gas temperature predictions. For the case of helium plasma discharge the gas temperature rise is not drastic due to the high thermal diffusivity of helium itself. As such discharges in helium gases are treated to be an exception. However discharges in diatomic gases such as nitrogen, oxygen and hydrogen are shown to have significantly higher gas temperature [37] which makes which makes conjugate heat transfer analysis more crucial for those types of high pressure discharges.

Electrode temperature predictions are depicted in figure 4.28. As mentioned earlier, the Dirichlet boundary simulation is unable to capture the cathode and anode temperature rise and also the temperature difference between anode and cathode. Cathode temperatures should be higher than anode temperature since most of the gas heating happens near the cathode. Figure 4.29 depicts the voltage current characteristics curve derived from CHT and Dirichlet boundary condition simulations. Gas temperature is the main reason for the decrease in the discharge voltage decrease over the normal glow evolution, since it rarifies the gas. Comparison between the two method's on discharge voltage predictions, shows that CHT simulation predicts lower V_d where the difference between two methods of simulation increases at the later stages of the normal glow discharge.

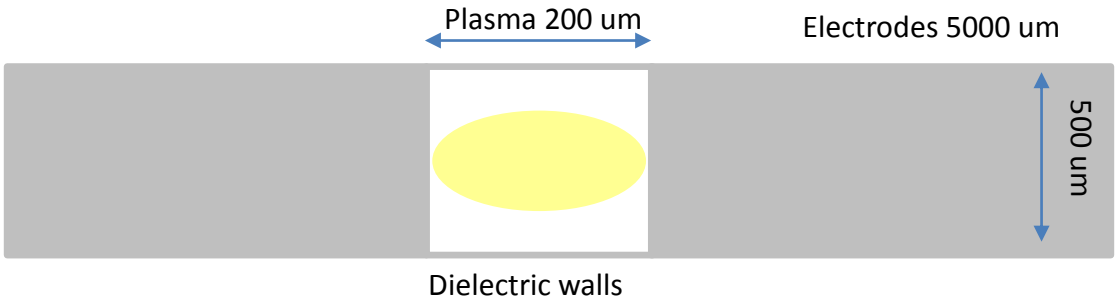

Figure 4.1. Schematic of the computational domain of the two dimensional simulations of the micro plasma discharge.

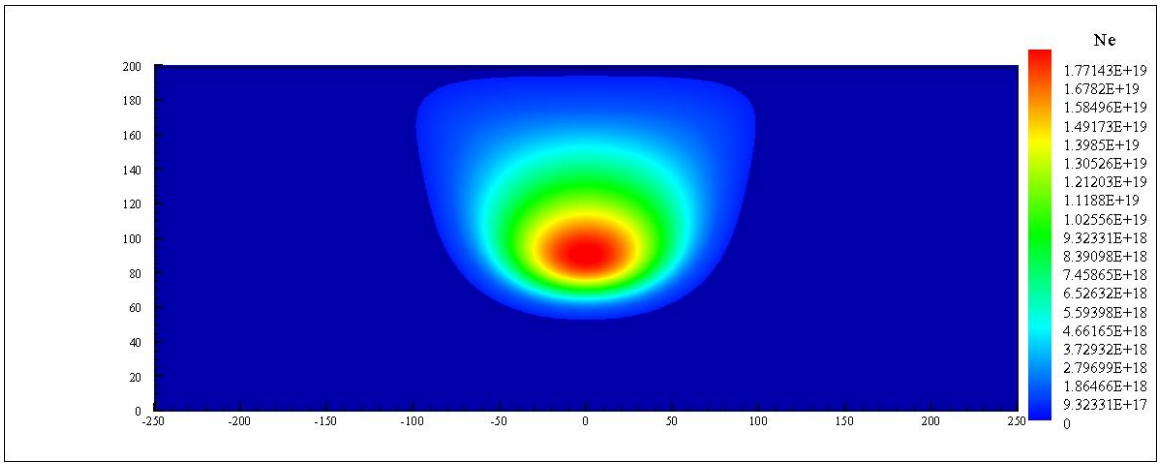

Figure 4.2. Electron density contour V_d~ 210 V, I_d= 0.1 mA, pd= 15.4 Torr.cm.

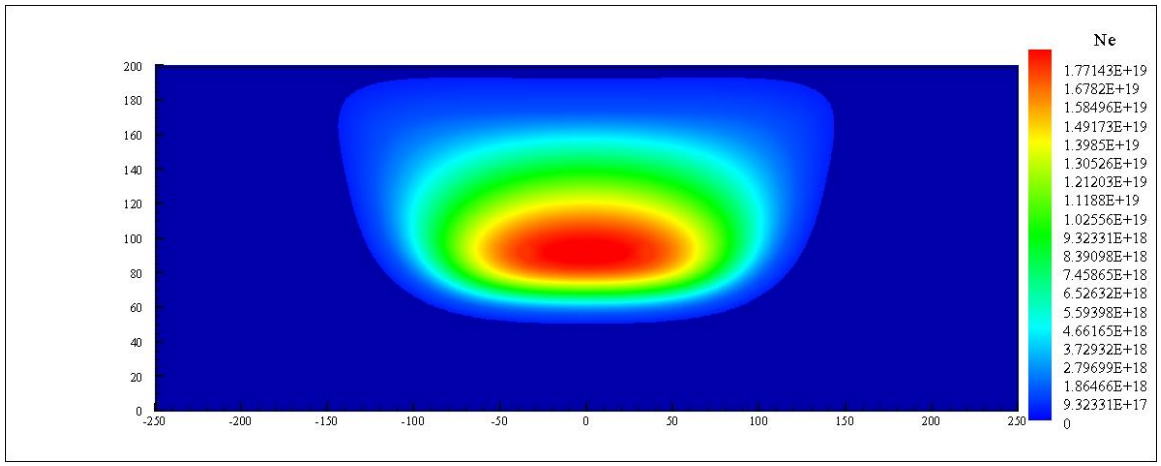

Figure 4.3. Electron density contour V_d~ 205 V, I_d= 0.3 mA, pd= 15.4 Torr.cm.

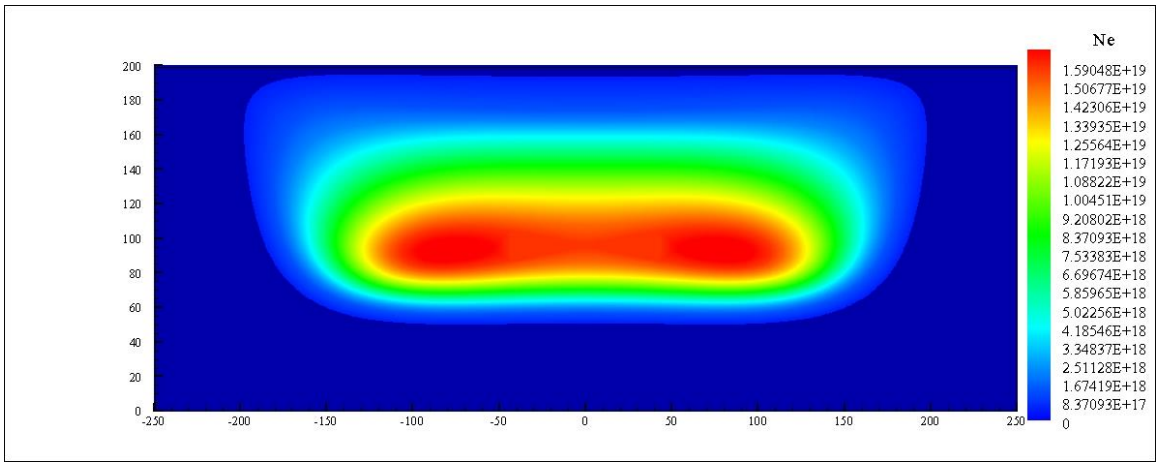

Figure 4.4 Electron density contour V_d~ 200 V, I_d= 0.5 mA, pd= 15.4 Torr.cm

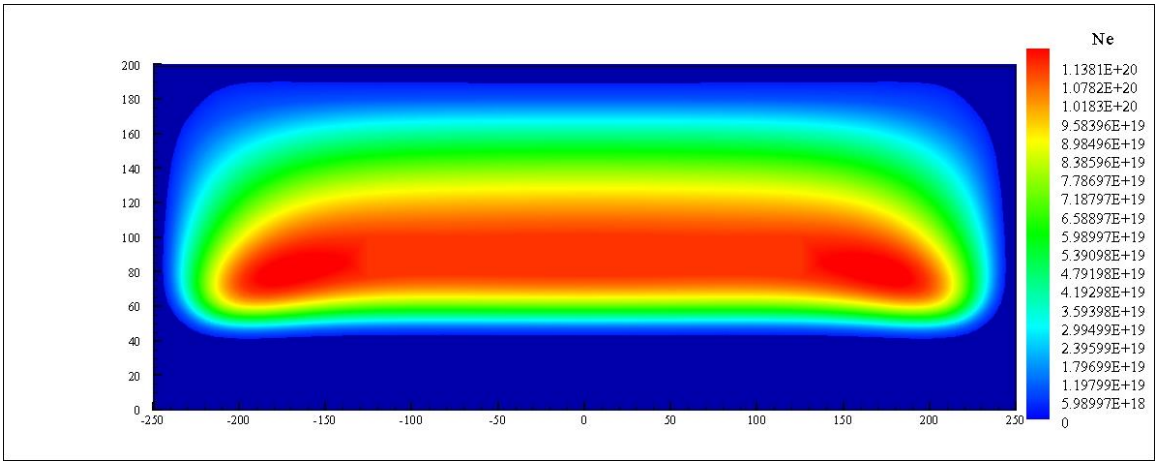

Figure 4.5. Electron density contour V_d~ 230 V, I_d= 1.5 mA, pd= 15.4 Torr.cm

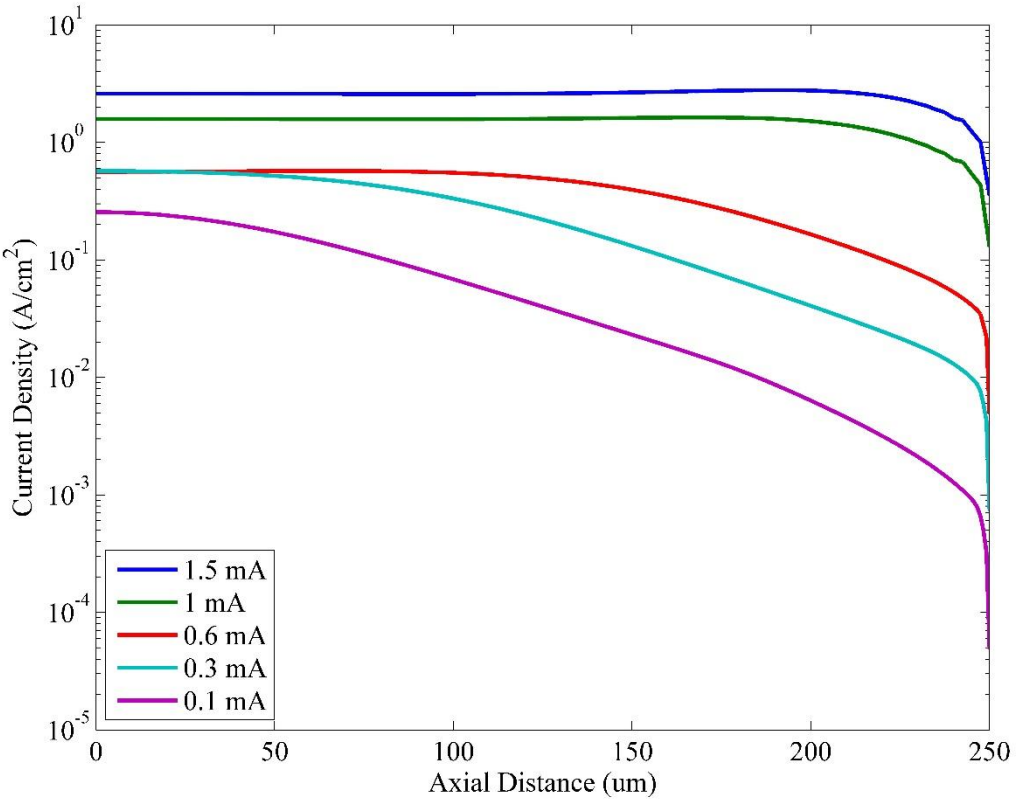

Figure 4.6. Radial ion current density distribution at the cathode surface for different discharge current (inter-electrode separation 200 um, atmospheric pressure)

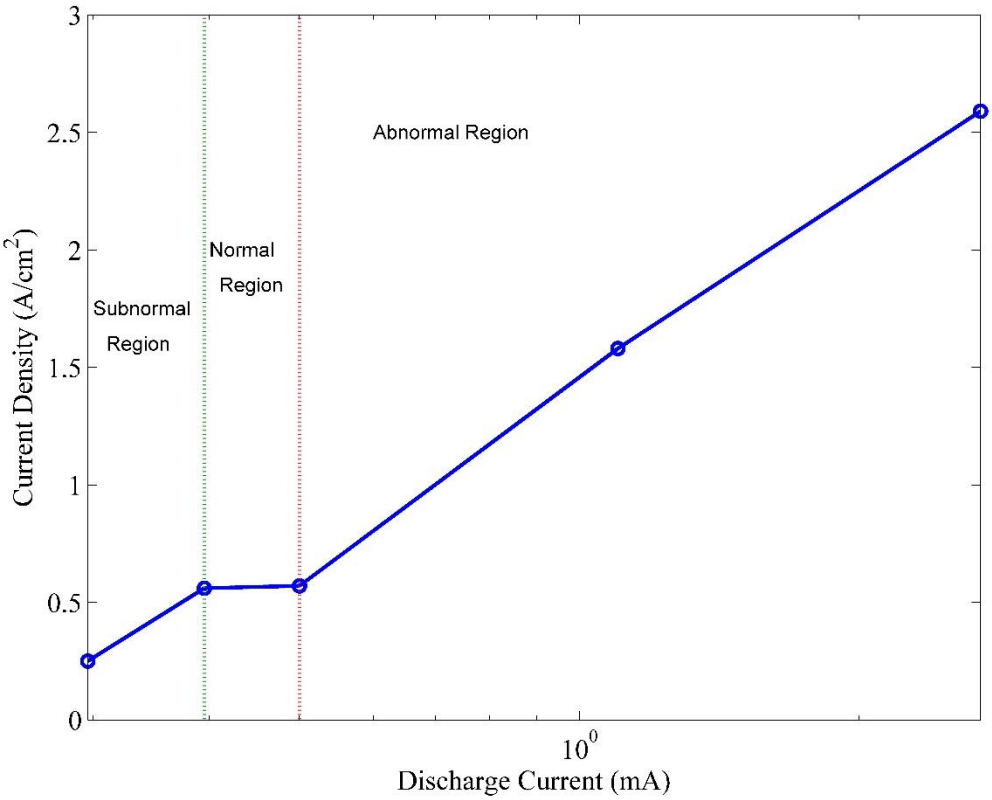

Figure 4.7. Current density evolution with total current (inter-electrode separation 200 um, atmospheric pressure).

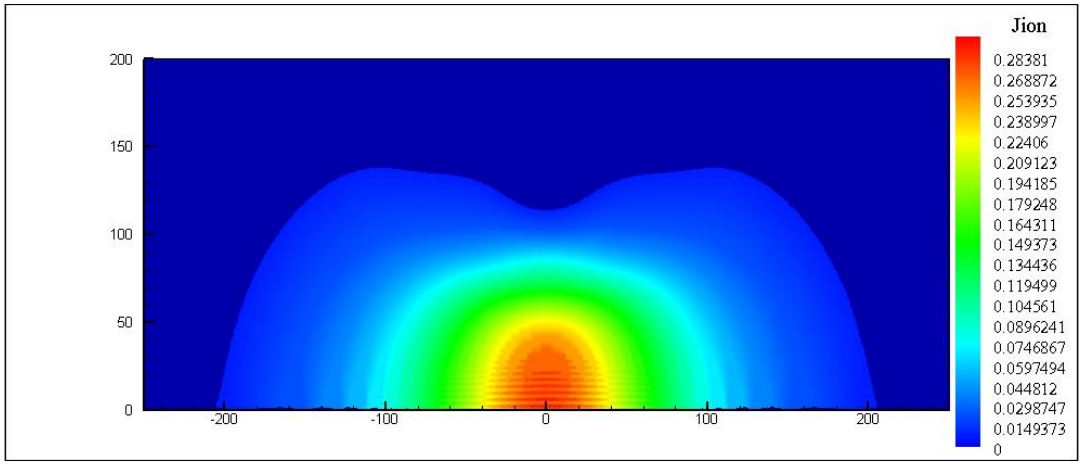

Figure 4.8 Ion current density contour V_d~ 200 V, I_d=1.5 mA, pd=15.4 Torr.cm

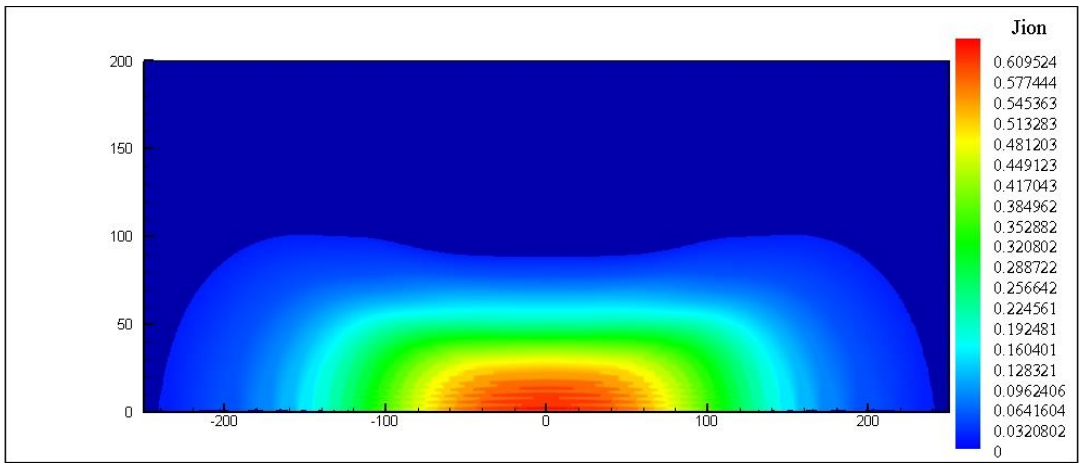

Figure 4.9. Ion current density contour V_d~ 200 V, I_d=1.5 mA, pd=15.4 Torr.cm

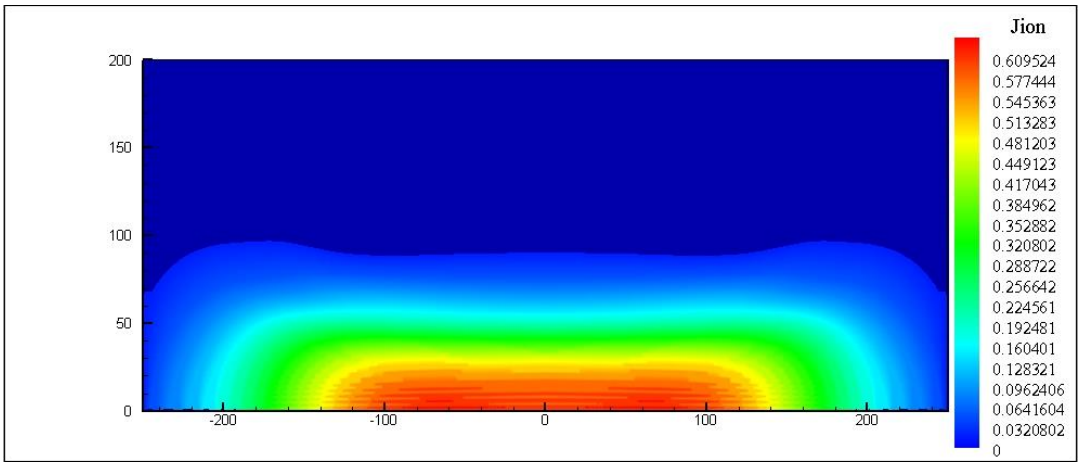

Figure 4.10. Ion current density contour V_d~ 205 V, I_d=1.5 mA, pd=15.4 Torr.cm.

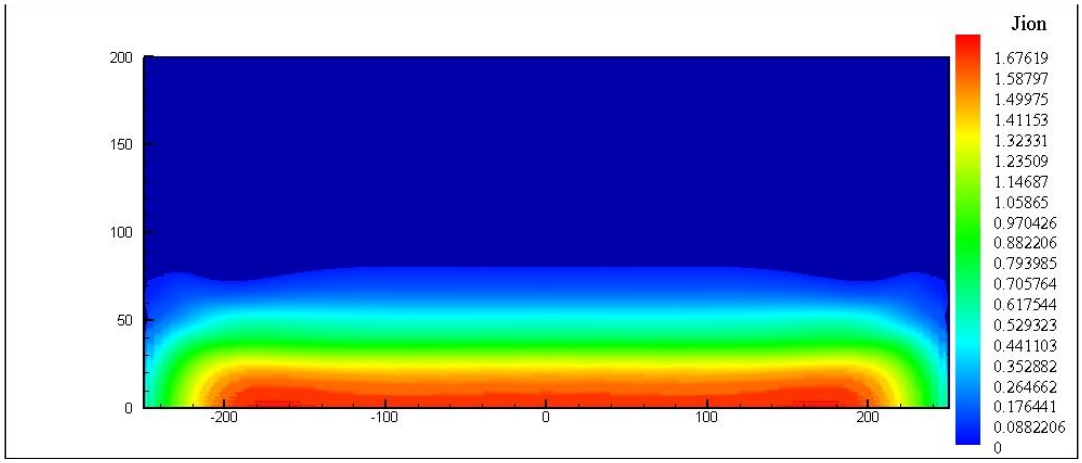

Figure 4.11. Ion current density contour V_d~ 230 V, I_d=1.5 mA, pd=15.4 Torr.cm

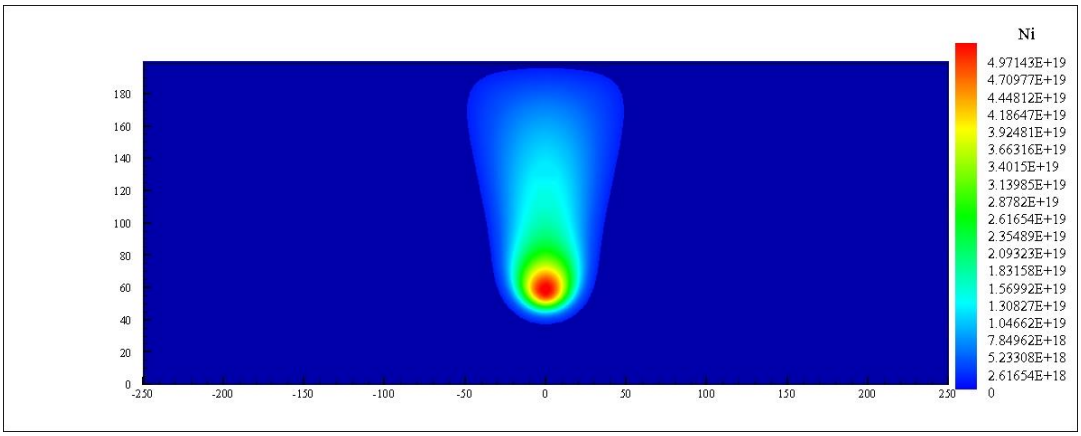

Figure 4.12. 2 atm electron density contour V_d~ 225 V, I_d= 0.1 mA, pd=30.8 Torr.cm.

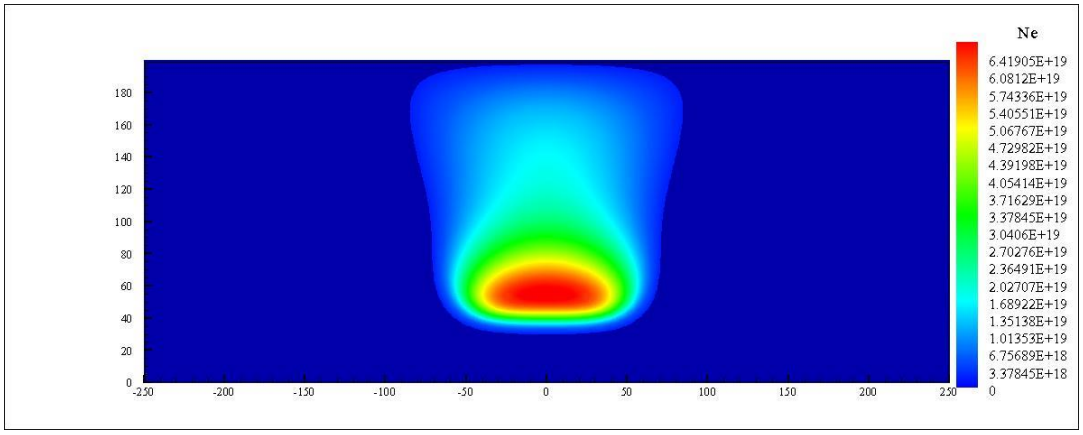

Figure 4.13. 2 atm electron density contour V_d~ 220 V, I_d= 0.5 mA, pd=30.8 Torr.cm.

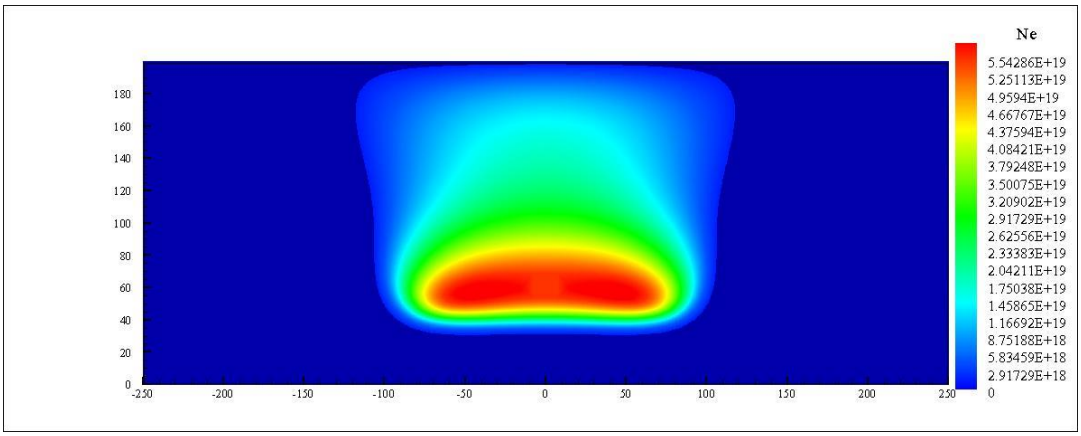

Figure 4.14. 2 atm electron density contour V_d~ 215 V, I_d= 1.0 mA, pd=30.8 Torr.cm.

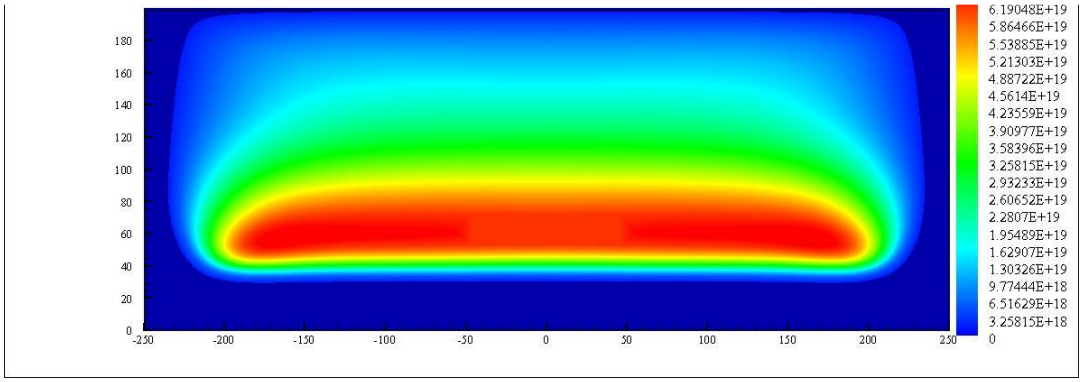

Figure 4.15. 2 atm electron density contour V_d~ 250 V, I_d= 3 mA, pd=30.8 Torr.cm.

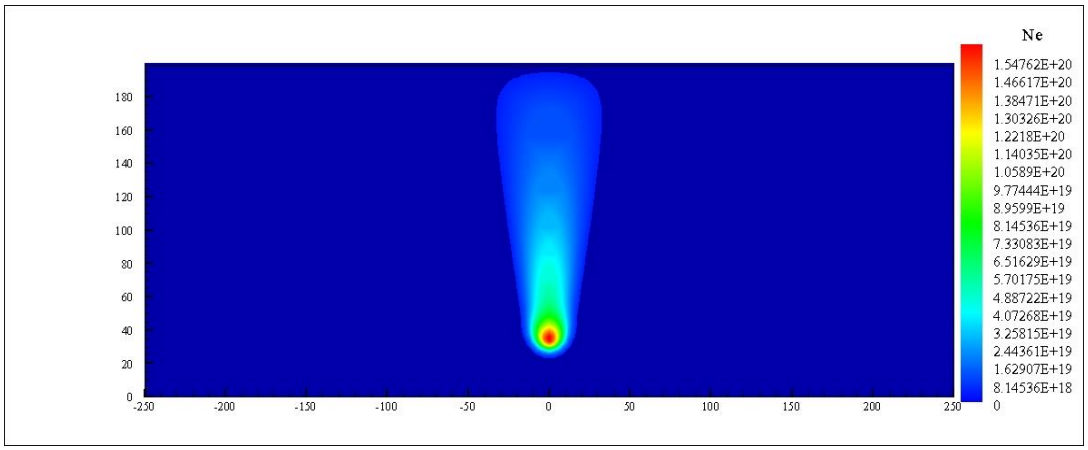

Figure 4.16. 4 atm electron density contour V_d~ 250 V, I_d= 0.1 mA, pd=61.6 Torr.cm.

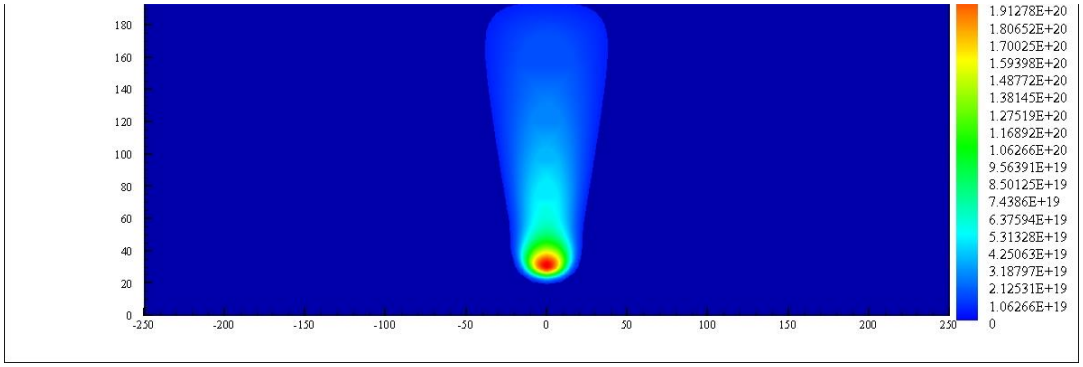

Figure 4.17. 4 atm electron density contour V_d~ 240 V, I_d= 1.0 mA, pd=61.6 Torr.cm.

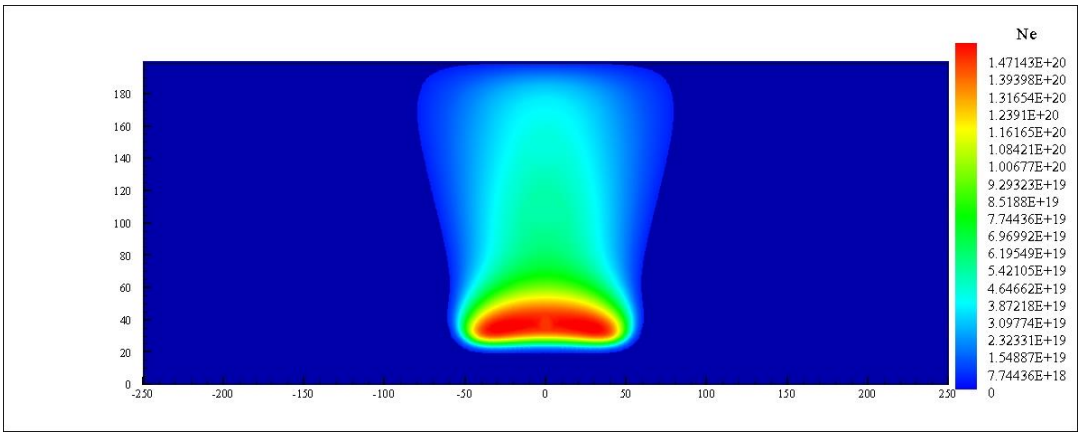

Figure 4.18. 4 atm electron density contour V_d~ 230 V, I_d= 5.0 mA, pd=61.6 Torr.cm.

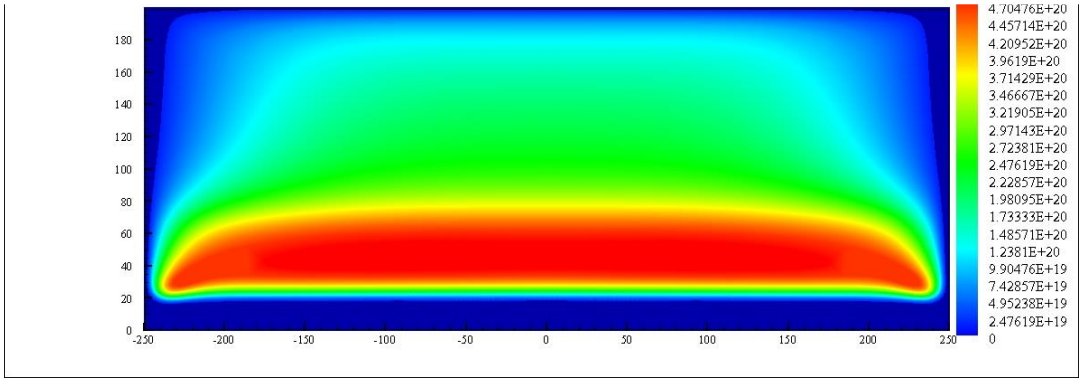

Figure 4.19. 4 atm electron density contour V_d~ 270 V, I_d= 12 mA, pd=61.6 Torr.cm.

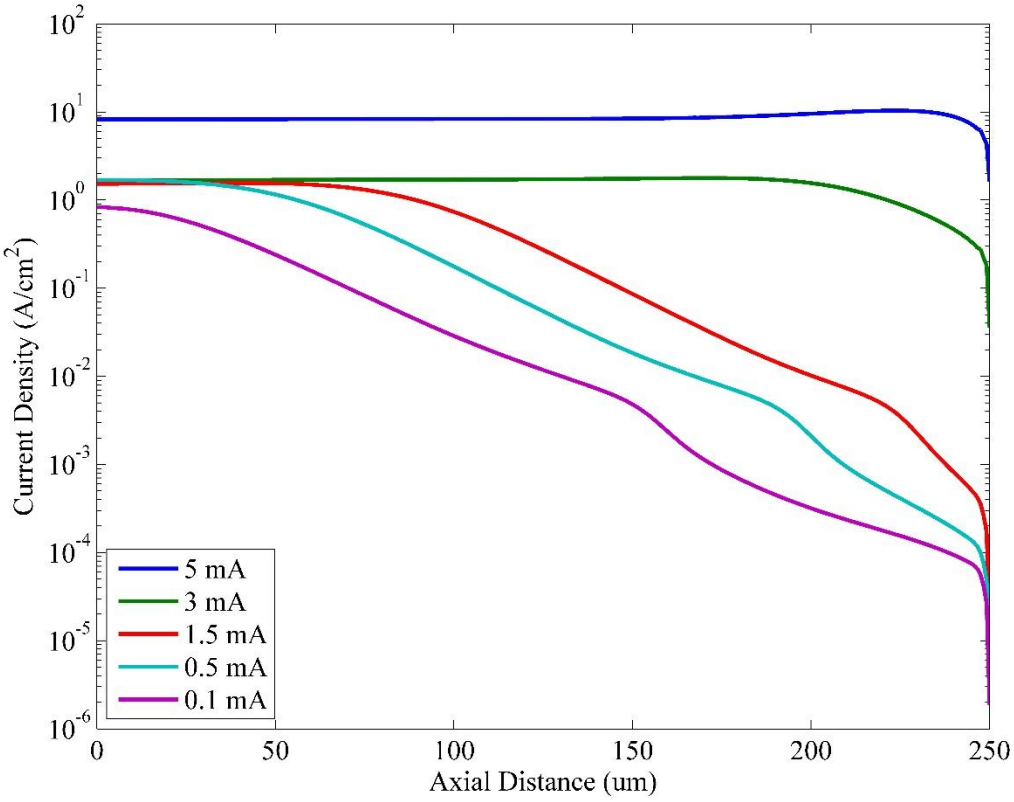

Figure 4.20. Radial ion current density distribution at the cathode surface for different discharge currents (inter-electrode separation 200 um, 2 atm).

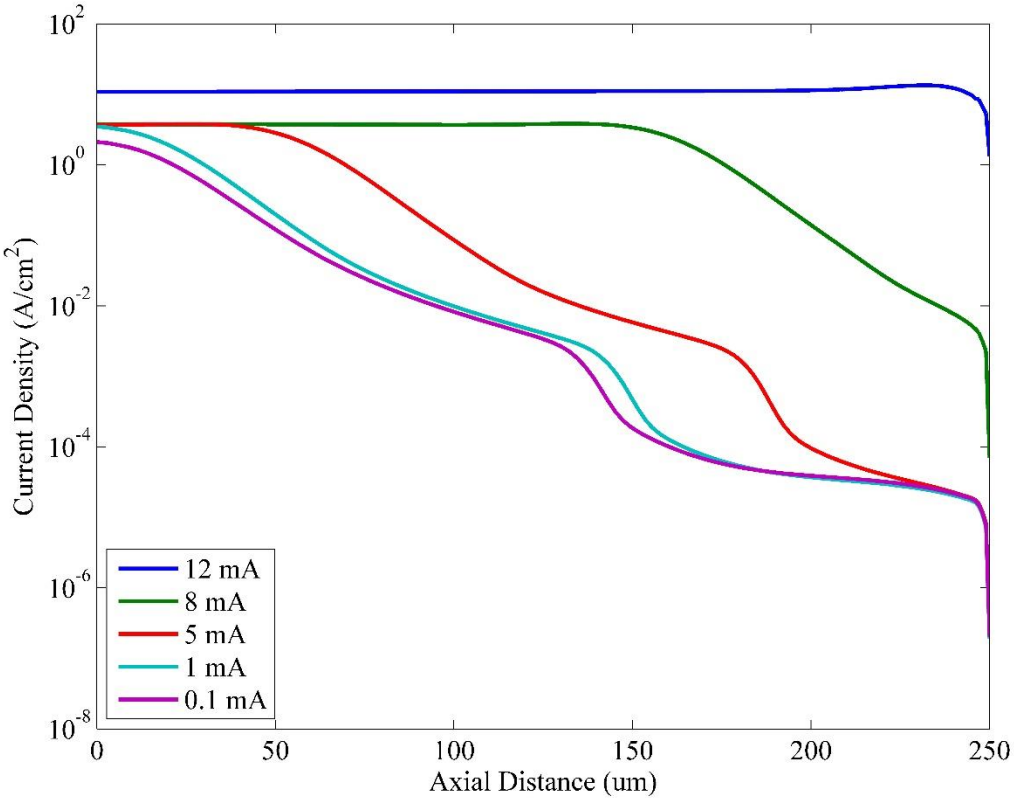

Figure 4.21. Radial ion current density distribution at the cathode surface for different discharge currents (inter-electrode separation 200 um, 4 atm).

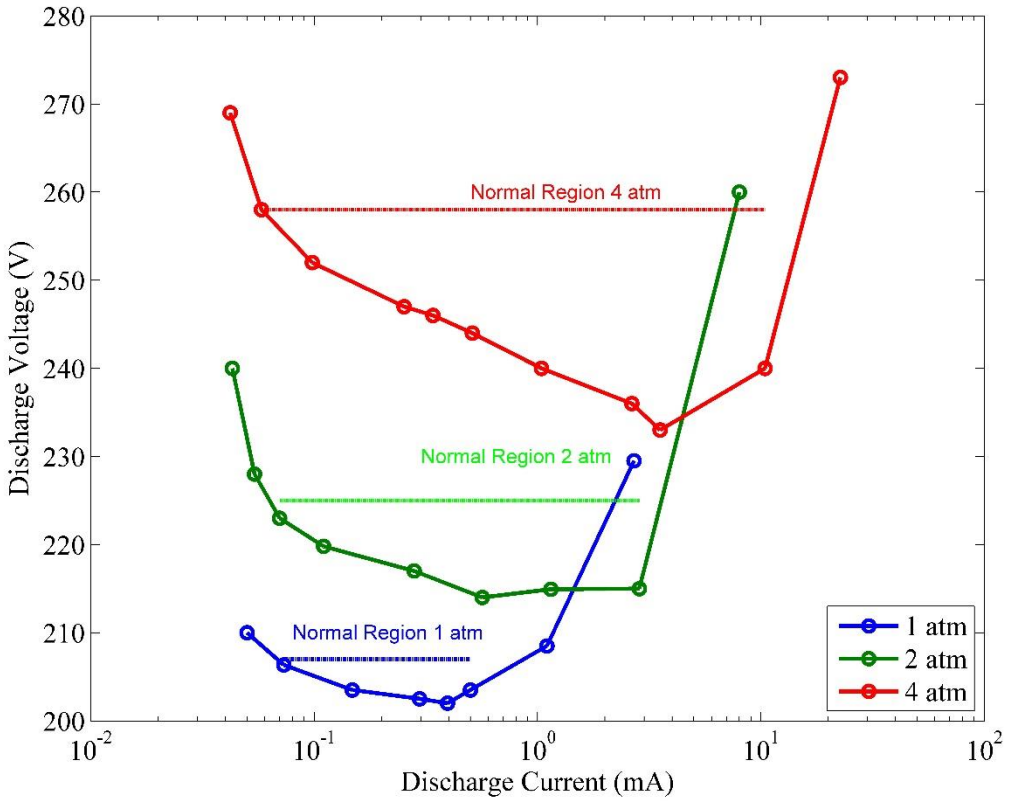

Figure 4.22. Voltage-current characteristics curve for different operating pressure.

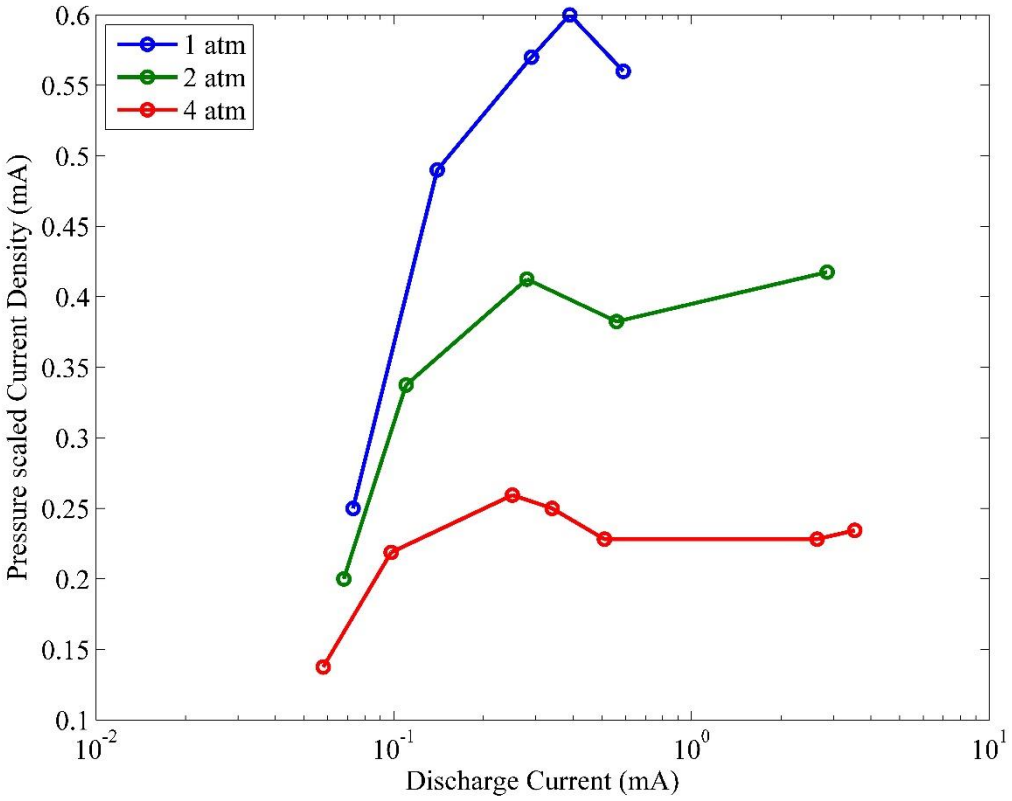

Figure 4.23. Pressure scaled voltage-current characteristics curve.

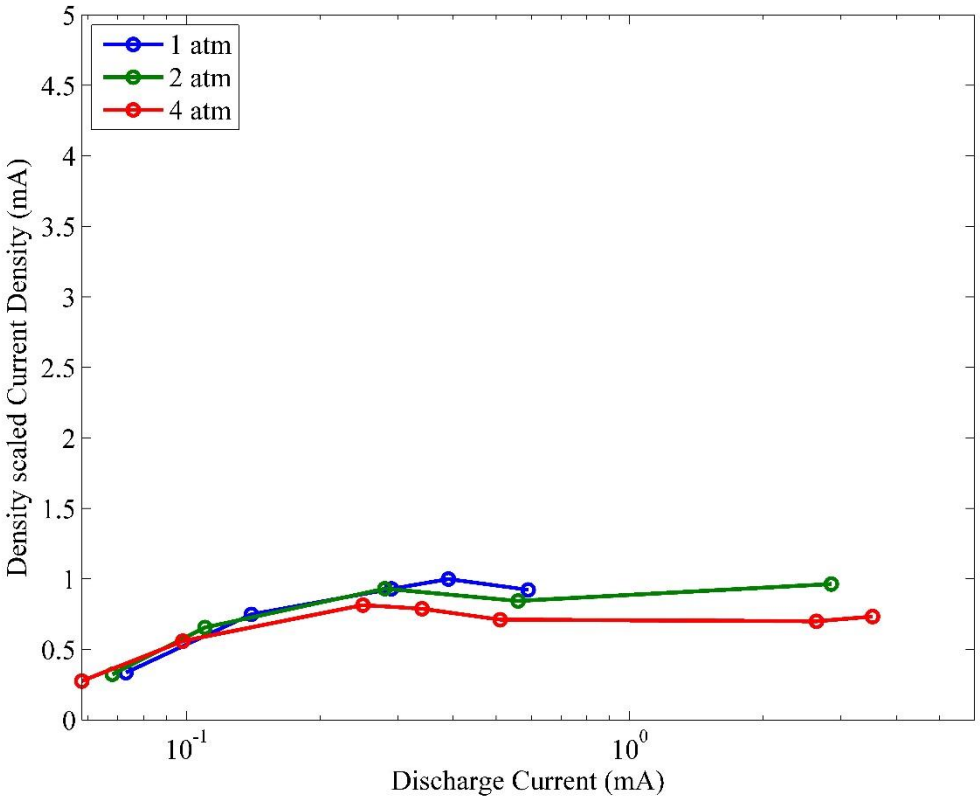

Figure 4.24. Density scaled voltage-current characteristics curve.

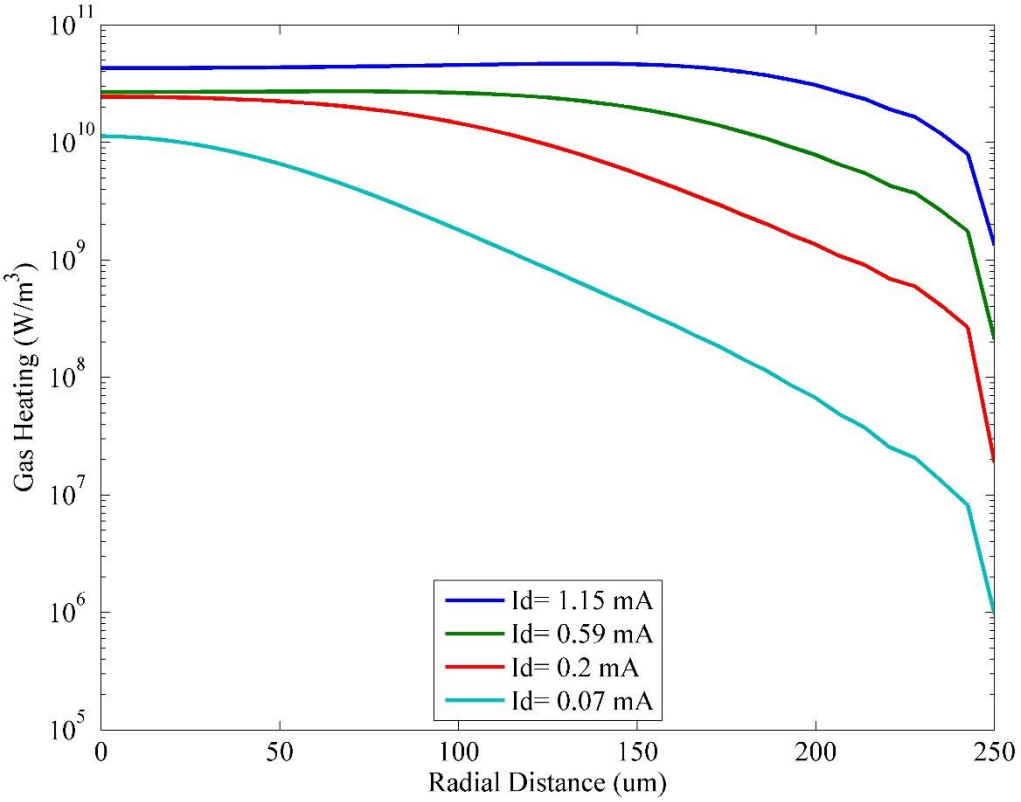

Figure 4.25 Radial distribution (x = 0) of neutral gas temperature source term at different discharge currents.

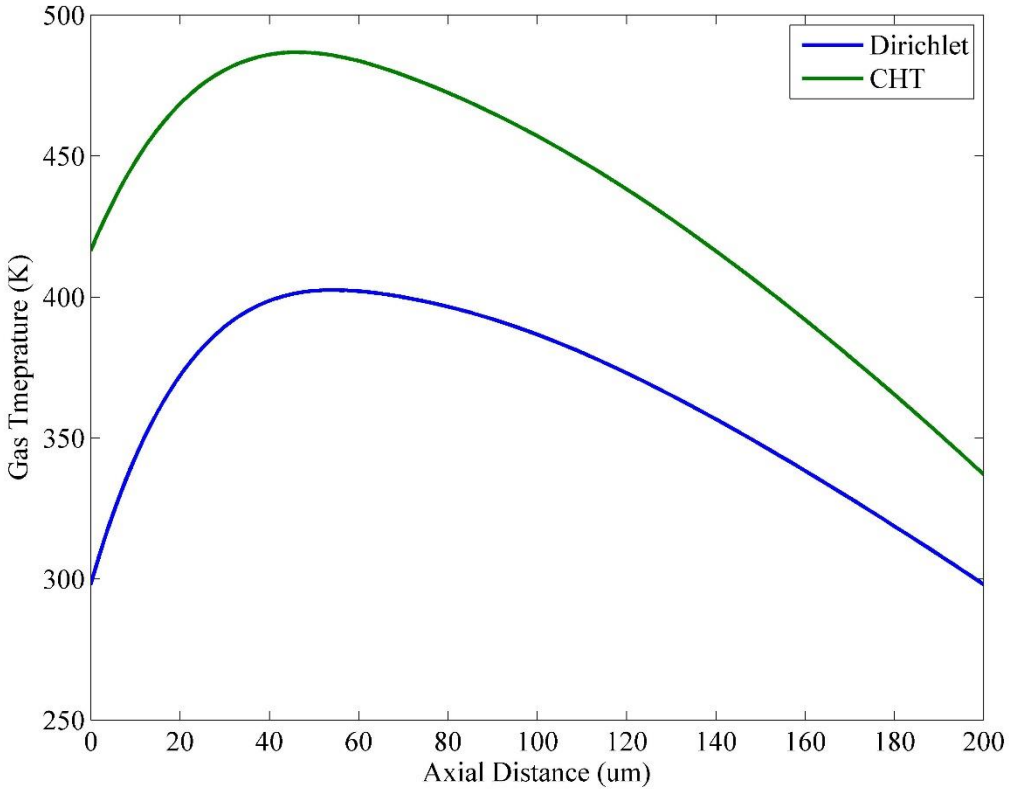

Figure 4.26. Spatial gas temperature distribution. Comparison of predictions between conjugate heat transfer and Dirichlet boundary conditions at atmospheric pressure.

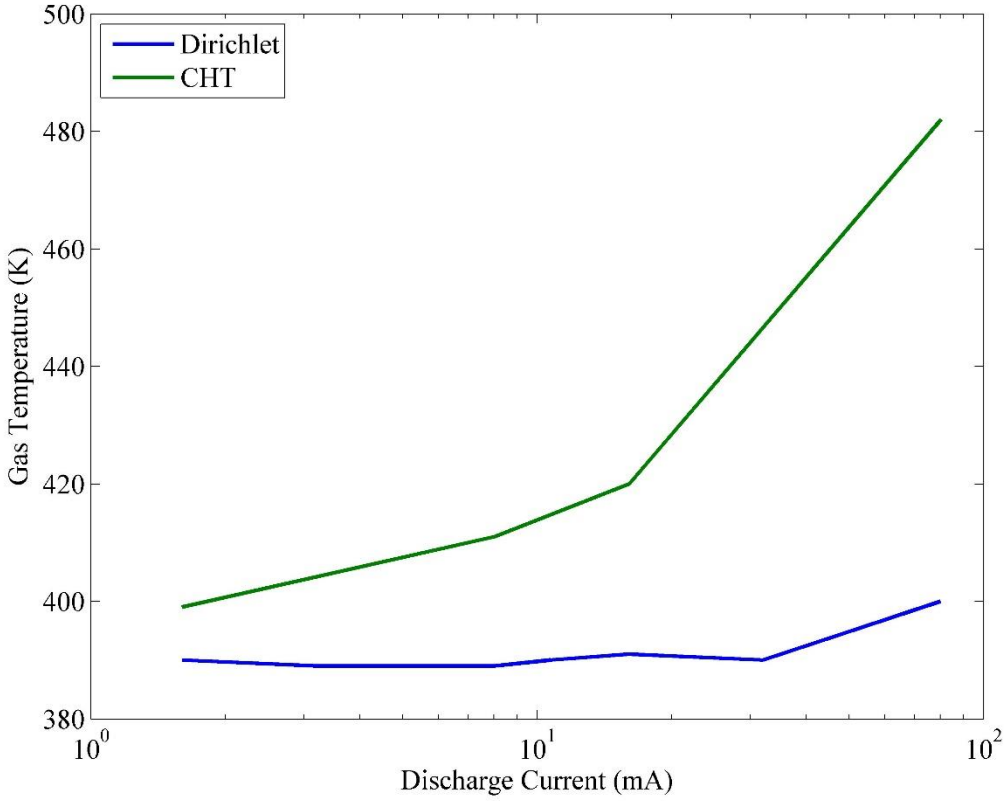

Figure 4.27. Peak gas temperature as a function of discharge current. Comparison of predictions between conjugate heat transfer and Dirichlet boundary conditions at atmospheric pressure.

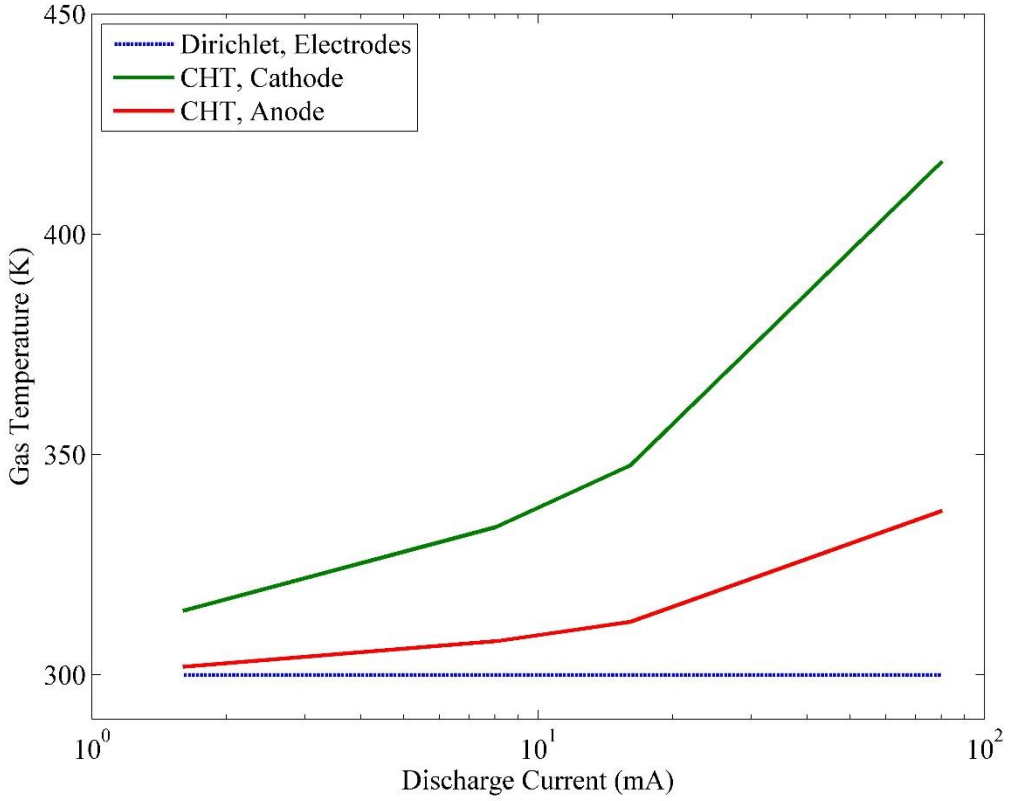

Figure 4.28. Wall temperature predictions, comparison between CHT analysis and Dirichlet boundary.

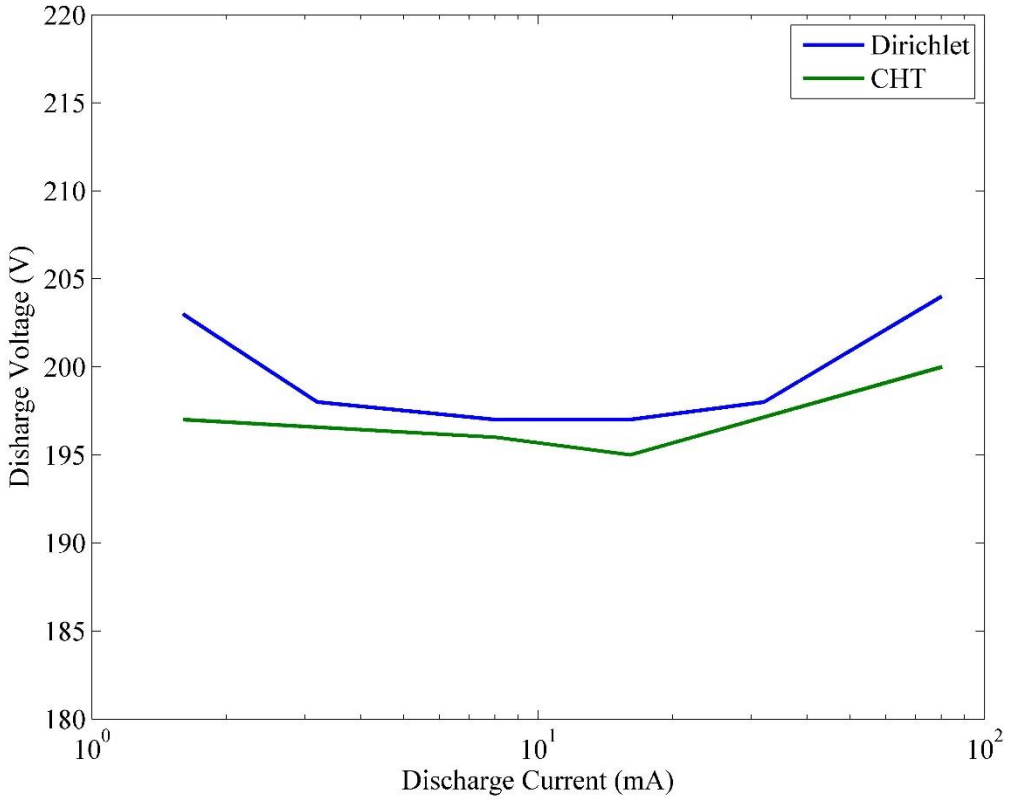

Figure 4.29. Voltage current characteristics curve, comparison between CHT analysis and Dirichlet boundary.

CHAPTER 5

CONCLUSION

Atmospheric-pressure Helium-Nitrogen (99.98% He and 0.02% N_2) dc micro glow discharge has been computationally investigated using a fluid model together with an external circuit. Simulations have been conducted for a parallel plate electrode configuration with an inter electrode spacing of 200 um. A dynamic time-stepping scheme (backward difference formula) has been employed to address the vastly different time scales associated with plasma and fluid transports as well as electrodes thermal properties.

A one-dimensional model has been employed to obtain the characteristics of the high pressure glow discharge. The voltage current characteristics curve for different input pressure was obtained by varying the ballast resistance. The rapidly increasing discharge voltage indicated the discharge is operating at the "*abnormal*" glow mode.

A conjugate heat transfer analysis was conducted to capture the varying temperature boundaries of the electrodes and eliminate the artificial temperature distribution forced by the conventional "*Isothermal*" boundary. At 4 mA the peak gas temperatures between the two model predictions were found to differ by ~300 K. consequentially the temperatures at the cathode and anode differed by ~ 400 K and 100 K respectively. Temperature predictions from the conjugate heat

transfer model was always found to be higher for identical conditions. *V-I* curve and the temperature distribution results were in favorable agreement with the experimental suggesting f that the "*isothermal*" boundary condition is unable to provide reliable results while representing realistic physics. The conjugate heat transfer analysis was found to be able to predict the effect of electrodes thermal properties on the discharge characteristics.

The extra computational overhead of conjugate heat transfer analysis was eliminated by implementing an approximate analytical solution for the wall temperatures. Instability and divergence caused by high rate of out ward heat flux temporal evolution was avoided by employing a "*Stepping method*". Electrodes temperature results and the *V-I* were found to be in a fine agreement with the experimental results obtained from literature [17].

A two dimensional model was employed to characterize the high pressure glow discharge. The voltage current characteristics curve for different input pressure was obtained by varying the ballast resistance. The constant current density indicated the discharge to be operating at the *"normal*" glow mode. The obtained current density was approximately found to be 0.6 $\frac{A}{cm^2}$ which is in fair agreement with experimental results available in the literature. "*Normal*" glow discharge voltage was found to scale with effective density in contrast to its low pressure counterpart where pressure alone is used as the scaling factor.

A conjugate heat transfer analysis was employed to eliminate the artificial cooling effects of "*isothermal"* boundaries. Peak gas temperature value was

found to show approximately 100 K difference between the two simulation methods for a discharge current of ~ 80 mA.

The model was able to capture all the characteristics of "*normal"* and "*abnormal*" helium-nitrogen glow discharge at atmospheric and higher pressures. The conjugate heat transfer analysis was able to overcome the limitation of the "*isothermal*" boundary. Implementing the conjugate heat transfer analysis increases the accuracy of the predictions.

Further studies should be investigated on the effects conjugate heat transfer analysis on high pressure micro plasma discharge using more detailed kinetics especially those of diatomic gases to obtain better plasma characteristics predictions.

REFERENCES

[1] Yu. P. Raizer, “Gas discharge physics” 1st edition, Springer (1991).

[2] B. Q. Yang, P.X. Feng, “A DC Plasma discharge source and its application to synthesis of carbon and carbon nitride thin films”, Surface Review and Letters, Vol. 14, No. 2 (2007) 309–314.

[3] H. S. Zhang, K. Komvopoulos, “Direct-current cathodic vacuum arc system with magnetic-field mechanism for plasma stabilization”, Review of scientific instruments, Vol. 79, 073905 (2008).

[4] D. P. Lymberopolous, D. J. Economou, “Fluid simulation of glow discharges”, J. Appl. Phys, Vol. 73, No. 8 (1993).

[5] H. R. Humud, A. S. Wasfi, W. A. Al-Razaq, “A Low Temperature Atmospheric Pressure Plasma Jet”, International Review of Physics (I.RE.PHY.), Vol. 7, N. 1 (2013).

[6] T.I. Farouk, B. Farouk, D. Staack, A. Gustol, A. Fridman, “Simulation of dc atmospheric pressure argon micro glow-discharge” Plasma Sources Sci. and Technol. Vol. 15, (2006), 676 – 634.

[7] T.I. Farouk ,B. Farouk, D. Staack, A. Gustol, A. Fridman, “Modeling of direct current micro-plasma discharge in atmospheric pressure hydrogen” Plasma Sources Sci. and Technol. Vol. 16 ,(2007), 619 – 634.

[8] R. B. Tyata, D. P. Subedi, R. Shrestha, C. S. Wong, “Generation of uniform atmospheric pressure argon glow plasma by dielectric barrier discharge”, Pranama Journal of Physics, Vol. 80, No. 3 (2013) 507–517.

[9] G. Y. Park, S. J. Park, M. Y. Choi, I. G. Koo, J. H. Byun, J. W. Hong, J. Y. Sim, G. J. Collins, J. K. Lee, “Atmospheric- pressure plasma sources for biomedical applications”, Plasma Sources Sci. and Technol. Vol. 21 (2012).

[10] X. Lu, M. Laroussi, V. Puech, “On atmospheric –pressure non-equilibrium plasma jets and plasma bullets”, Plasma Sources Sci. and Technol., Vol. 21, No. 3 (2012).

[11] Q. Wang, D.J. Economou, V. M. Donnelly, “Simulation of direct current micro plasma discharge at atmospheric pressure” J. of Appl. Phys. 100, (2006), 023301. 1 – 10.

[12] J. Janasky, Q.T. Algwari, D. O’connell, A. Bourdon, “Experimental-modeling study of an atmospheric-pressure helium discharge propagating in a thin dielectric tube” IEEE transactions on plasma science, Vol. 40, (2012),11

[13] J. S. Shanga, P. G. Huang, “Modeling of ac dielectric barrier discharge”, J. of Appl. Phys., Vol. 107, (2010).

[14] A. Fridman, L.A. Kennedy, “Glow Discharge” in Plasma Physics and Engineering, 2nd edition, CRC Press (2011).

[15] L. Tong, “Simulation of an Atmospheric Pressure Direct Current Micro plasma Discharge in He/N2”, COMSOL conference, Boston (2011).

[16] Q. Wang, D.J. Economou, V. M. Donnelly, “Simulation of direct current micro plasma discharge at atmospheric pressure” J. of Appl. Phys. 100, (2006), 023301. 1 – 10.

[17] Q. wang, I. Koleva, V. Donnelly, D. Economou, “Spatially resolved diagnostics of an atmospheric pressure direct current helium microplasma”, J. Phys. D: Appl. Phys. 38 (2005) 1690–1697.

[18] Y. Yener , S. Kakac, “Heat Conduction”, 4th edition, CRC Press (2008) , 86-93, 320-335.

[19] F. Incropera, D. DeWitt, “Fundamentals of Heat and Mass Transfer”, 5th edition, John Wiley and Sons.

[20] V. Guerra, P.A. Sa, J. Loureiro, “Kinetics modeling of low-pressure nitrogen discharge and post-discharge”, Eur. Phys. J. Appl. Phys. 28 (2004), 125-152.

[21] Q. wang, I. Koleva, V. Donnelly, D. Economou, “Spatially resolved diagnostics of an atmospheric pressure direct current helium microplasma”, J. Phys. D: Appl. Phys. 38 (2005) 1690–1697.

[22] D. Staack, B. Farouk, A. Gustol, A. Fridman, “DC normal glow discharges in atmospheric pressure atomic and molecular gas”, Plasma Sources Sci. Technol. 17(2008)025013

[23] D. Staack, B. Farouk, A. Gustol, A. Fridman, “Characterization of a dc atmospheric pressure normal glow discharge”, Plasma Sources Sci. Technol. 14(2005)700-711.

[24] S. Pantazis, J. Buthig, K. Jouston, “Conjugate heat transfer simulations of a thermocouple sensor in a low temperature nitrogen gas ambient”, International Journal of Heat and Mass Transfer 70 (2014) 536-544.

[25] S. Fontanesi, M. Giacopini, “Multiphase CFD-CHT optimization of the cooling jacket and FEM analysis of the engine head of a V6 diesel engine”, Applied Thermal Engineering 52 (2013) 293-303.

[26] F. Duchaine, A. Corpron, L. Pons, V. Moureau, F. Nizoud, T. Poinsot, “Development and assessment of a coupled strategy for conjugate heat transfer with large eddy simulation: application to a cooled turbine blade”, Internation Journal of Heat and Fluid Flow 30 (2009) 1129-1141.

[27] A. Veeraragavan, C. P. Cadou, “Flame speed predictions in planar micro/mesoscale combustors with conjugate heat transfer”, Combustion and Flame 158 (2011) 2178-2187.

[28] A. Veeraragavan, C. P. Cadou, “Theoretical study of conjugate heat transfer effects on temperature profiles in parallel flow with embedded heat sources”, International Journal of Heat and Mass Transfer 53 (2010) 1699-1711.

[29] C. Shen, F. Sun, X. Xia, “Analysis on transient conjugate heat transfer in gap-cavity-gap structure heated by high speed flow”, International Journal of Heat and Mass Transfer 67 (2013) 1030-1038.

[30] B. Ramamurthi, D. J. Economou and I. D. Kaganovich, “Effect of electron energy distribution function on power deposition and plasma density in an inductively coupled discharge at very low pressures” Plasma sources science and technology, 12 (2003) 302-312.

[31] M.D. Smooke, “Solution of burner-stabilized premixed laminar flames by boundary value method”, Journal of Computational Physics, 48, 72-105 (1982).

[32] P.D. Neufeld, A.R. Janzen, and R.A. Aziz, J. Chem. Phys., vol. 57, p. 1100, 1972.

[33] COMSOL Multi Physics, Burlington, MA 01803 USA.

[34] A. V. Phelps, “Abnormal glow discharge in Ar: experiments and models”, Plasma Sources Sci. Technol. 10 (2001) 329-343.

[35] T. Farouk, B. Farouk, A. Fridman, “Computational Studies of Atmospheric-Pressure Methane–Hydrogen DC Micro Glow Discharges”, IEEE Transactions on plasma science, 38 (2010), 73-85.

[36] V. I. Arkhipenko, A. A. Kirillov, Ya. A. Safronau, L. V. Simonchik and S. M. Zgirouski, “Self-sustained dc atmospheric pressure normal glow discharge in helium: from micro amps to Amps”, Plasma Sources Sci. Technol. 18 (2009) 045013.

[37] D. Staack, B. Farouk, A.F. Gutsol, A. Fridman, “Spatially Resolved Temperature Measurements of Atmospheric-Pressure Normal Glow Microplasmas in Air”, IEEE Transaction on Plasma Sciecne, 35 (2007) 1448 – 145